Title

Preference of CAMSAP3 for expanded microtubule lattice contributes to stabilization of the minus end

Author

Hanjin Liu[1], Tomohiro Shima[1,2]

Affiliation

1. Department of Biological Sciences, Graduate School of Science, The University of Tokyo

Hongo 7-3-1, Bunkyo-ku, Tokyo #113-0033, JAPAN

2. Corresponding author,

T. S. Tel: +81 (0) 3 5841 4399, Email: tomohiro.shima@bs.s.u-tokyo.ac.jp

Running title

Preference of CAMSAP3 and expansion of microtubule lattice

Keywords

Cytoskeleton, polymorphism, lattice expansion, MAPs,

Summary blurb

D2 region in CAMSAP3 preferentially bound to expanded microtubule lattices and also induced lattice expansion, explaining the molecular functions of CAMSAP3.

Abstract

CAMSAPs are proteins that show microtubule minus-end-specific localization, decoration and stabilization. Although the mechanism for minus-end recognition via their C-terminal CKK domain has been well described in recent studies, it is unclear how CAMSAPs stabilize microtubules. Our several binding assays revealed that D2 region of CAMSAP3 specifically binds to microtubules with the expanded lattice. To investigate the relationship between this preference and the stabilization effect of CAMSAP3, we precisely measured individual microtubule lengths and found that D2-binding expanded the microtubule lattice by ~3%. Consistent with the notion that the expanded lattice is a common feature of stable microtubules, the presence of D2 slowed the microtubule depolymerization rate to approximately 1/20, suggesting that the D2-triggered lattice expansion stabilizes microtubules. Combining these results, we propose that CAMSAP3 stabilizes microtubules by lattice expansion upon D2-binding, which further accelerates the recruitment of other CAMSAP3 molecules. Since only CAMSAP3 has D2 and the highest microtubule stabilizing effect among mammalian CAMSAPs, our model also explains the molecular basis for the functional diversity of CAMSAP family members.

Introduction

Microtubules are a eukaryotic cytoskeletal polymer with a hollow cylindric structure composed of α- and β-tubulin heterodimers (Zhang *et al*., 2018). They play essential cellular roles such as providing mechanical strength, building the machinery for cell division, and working as the railway on which motor proteins transport intracellular components (Dent *et al*., 2014; Goodson and Jonasson, 2018). Microtubules change their spatio-temporal distributions in cells in response to biochemical signals to construct the basic machinery for mitosis, cellular development and migration (Gadde and Heald 2004; Williamson *et al*., 1996; Dogterom and Koenderink, 2019). This dynamic reorganization is achieved mainly by two phenomena: polymerization/depolymerization and nucleation. Polymerization and depolymerization refer to the addition/removal of tubulin dimers at pre-existing microtubule tips, which results in microtubule elongation and shrinkage, respectively, a phenomenon usually called dynamic instability (Mitchison and Kirschner, 1984). On the other hand, microtubule nucleation generates new microtubules from tubulin dimers (Job *et al*., 2003; Ayukawa *et al*., 2021). The fine regulation of dynamic instability and nucleation is important for keeping microtubule networks ordered in cells and thus for proper cell activities.

Eukaryotes have a huge number of microtubule-associated proteins (MAPs) that alter microtubule dynamics. For instance, microtubule end-tracking proteins EB1 and XMAP215 increase the microtubule growth rate and catastrophe frequency, promoting microtubule dynamic instability (Zanic *et al*., 2013; Farmer *et al*., 2021), whereas cytoplasmic linker-associated proteins (CLASPs) protect microtubules from depolymerization and suppress catastrophe (Aher *et al*., 2018). Among MAPs, calmodulin-regulated spectrin-associated proteins (CAMSAPs) and the invertebrate homolog patronin track the microtubule minus end and regulate microtubule dynamics (Hendershott *et al*., 2014; Jiang *et al.*, 2014; Akhmanova and Steinmetz, 2019). Patronin/CAMSAPs are also hypothesized to be non-centrosomal microtubule nucleators, thus providing an indispensable role in cells that need microtubules to be nucleated far from the cell centrosome (Meng *et al*., 2008; Goodwin and Vale, 2010; Tanaka *et al*., 2012; Feng *et al*., 2019; Imasaki et al., 2022). In cells, mutations or knockdown of CAMSAPs disturb microtubule growth or patterning, reaffirming the importance of these proteins in microtubule organization (Tanaka *et al*., 2012; Toya *et al*., 2016; Pongrakhananon *et al*., 2018; Coquand *et al*., 2021).

Vertebrates generally have three CAMSAP members, CAMSAP1-3, which show slight differences in their interactions and functions with microtubules. *In vitro* experiments using mouse CAMSAPs found that CAMSAP1 can track the microtubule minus tip but does not affect microtubule dynamics. On the other hand, CAMSAP2 not only tracks the microtubule minus tip but remains bound to the microtubule after minus end elongation, resulting in microtubule decoration at the larger area of minus ends. It also stabilizes microtubules and protects microtubules from catastrophe. Finally, CAMSAP3 decorates and stabilizes microtubule minus ends, with a stronger effect than CAMSAP2. CAMSAPs consist of several coiled-coil regions and a well-conserved C-terminal globular domain called CKK (Atherton *et al.*, 2017) that is responsible for the minus-end specificity of the proteins. Recent structural studies on the CKK domain have revealed how the CKK domain recognizes slight structural differences between microtubule minus ends and other regions (Atherton *et al*.,

2017; Atherton *et al*., 2019). However, these studies investigated the CKK domain only and failed to clarify the mechanism of the microtubule stabilization by CAMSAP2/3 and why CAMSAP1 does not have this property.

To understand the microtubule stabilization mechanism, it is necessary to consider the structure of not only CAMSAPs but of microtubules too. Recent cryogenic electron microscopy (cryo-EM), X-ray diffraction and fluorescence microscopy studies have shown that microtubules can take diverse conformations depending on their binding states with nucleotides, proteins, and chemical agents. In terms of microtubule stability, the lattice expansion/compaction of the tubulin periodicity along the longitudinal axis shows a clear correlation. The inhibition of microtubule depolymerization by the very slowly hydrolysable nucleotide guanosine-5'-[(α, β)-methyleno]triphosphate (GMPCPP), treatment with the anti-cancer drug taxol (Alushin *et al.*, 2014; Kamimura *et al.*, 2016), or mutations in the GTPase site (LaFrance *et al.*, 2022) force microtubules to take conformations with the expanded lattice compared to the unstable GDP-bound state. Therefore, lattice expansion is thought to be a common conformational change needed for microtubule stabilization.

The lattice expansion/compaction provides a flexible way to control microtubule stability and is recognized by MAPs. The cell division master regulator TPX2 (Roostalu *et al.*, 2015) and motor protein KIF5C (Nakata *et al.*, 2011; Morikawa *et al.*, 2015) can "read" the differences in microtubule conformations and preferentially bind to the expanded lattice. Interestingly, more recent studies have shown that both TPX2 and KIF5C actively introduce lattice expansion to compact microtubules or, in other words, "write" structural code on the microtubule and stabilize it upon their binding (Zhang *et al.*, 2017; Shima *et al.*, 2018; Peet *et al.*, 2018). Considering the "reading" and "writing" abilities are conferred to KIF5C and TPX2 in a conjugative manner, it may be common for "reader" proteins to work as "writers" as well and stabilize microtubules through lattice expansion. Because preferential binding to the expanded lattice implies that the expanded lattice is energetically favorable for the "reader"-microtubule complex, this difference in free energy may be the driving force that expands the compact lattice.

The discovery of "reader/writer" MAPs raises the possibility that a similar "reader/writer" region exists in CAMSAP2/3 but not CAMSAP1. Truncation studies of CAMSAPs have demonstrated that CAMSAP2/3 have regions that, unlike the CKK domain, bind to the expanded lattice of GMPCPP-stabilized microtubule seeds but hardly bind to the compact lattice of dynamically polymerized GDP-bound microtubules (Jiang *et al*., 2014; Atherton *et al*., 2017). These truncated constructs have included the middle region, named microtubule binding domain (MBD), or region adjacent to the CKK domain, named D2, for which little is known (see Fig. S1 of Atherton *et al*., 2017). Because these regions seem to "read" the expanded lattice, we hypothesized they play a key role in stabilizing microtubules.

Here, we investigated the D2 region, which has 139 residues, of human CAMSAP3 for its contribution to microtubule stabilization. Our series of *in vitro* experiments revealed that D2 has a high affinity for various types of microtubules with the expanded lattice, including GMPCPP-stabilized, taxol-stabilized and KIF5C-pre-treated GDP-microtubules. Consistent with our hypothesis, an excess amount of D2 expanded the lattice of GDP-microtubules and inhibited depolymerization. These results strongly suggest that D2 shares similar lattice "reader/writer" abilities with KIF5C and, therefore, can regulate microtubule dynamics upon its binding. The

111 synergy between the properties of D2 and the minus-end tracking ability of the CKK domain provides a common
112 explanation for the complex physiological roles of CAMSAPs.
113

3. Results

D2 region of human CAMSAP3 preferentially binds to GMPCPP-stabilized microtubules.

Previous *in vitro* microtubule dynamics assays have shown that the D2 region of mouse CAMSAP3 decorates microtubule seeds (Atherton *et al*., 2017). Since the microtubule seeds were composed of GMPCPP-bound tubulin, these results implied that the D2 region has a preference for GMPCPP-stabilized microtubules over standard GDP-bound microtubules (polymerized with GTP and hydrolyzed to GDP).

To verify if the same microtubule preference also holds for our D2 construct from human CAMSAP3, we conducted the binding assay using non-dynamic microtubules under total internal reflection fluorescence (TIRF) microscopy. The D2 region conjugated with fluorescent protein mCherry (D2-mCherry) was expressed and purified from *E. coli* using a histidine tag (Fig. 1A; Fig. S1). GDP-bound microtubules (GDP-MT) were polymerized from GMPCPP-bound microtubules (GMPCPP-MT) immobilized on the glass surface by biotin/avidin conjugation (Fig. 1B). In our assay, we did not immobilize GMPCPP-MT and GDP-MT separately for two reasons. First, when microtubules are spontaneously nucleated without seeds, the majority of GMPCPP-MT (80–96%) forms a 14-protofilament conformation, whereas GDP-MT shows a wide distribution of protofilament numbers (Hyman *et al.*, 1995; Rai *et al*., 2021). Therefore, to reduce the impact of the protofilament number, GDP-MT was polymerized from GMPCPP-MT to increase the ratio of 14-protofilament GDP-MT. Second, to analyze the structural transition of the GDP-MT lattice, we needed to eliminate the direct immobilization of GDP-MT on the glass surface, because the biotin/avidin immobilization may compete with and prevent the longitudinal expansion and/or skewing of the GDP-MT lattice. We avoided this problem by indirectly immobilizing GDP-MT via GMPCPP-MT. Thus, using this assay system, we observed D2-binding on GDP- and GMPCPP-MT. As expected, D2 specifically decorated GMPCPP-MT (Fig. 1C) but hardly bound to GDP-MT at D2 concentrations as high as 1 μM. Quantification of the fluorescence images showed exclusive binding on GMPCPP-MT at 0.25 μM D2 (GMPCPP-MT: 24 ± 6 a.u., GDP-MT: -0.6 ± 1.3 a.u.; mean ± S.D.) and 11-times higher affinity on GMPCPP-MT at 1 μM D2 (GMPCPP-MT: 78 ± 16 a.u., GDP-MT: 7.2 ± 4.9 a.u.; mean ± S.D.) (Fig. 1D). Thus, we confirmed that D2 prefers GMPCPP-MT and is a common feature of mouse and human CAMSAP3.

Affinity of D2 to microtubules increases in the presence of taxol

The preference of D2 to GMPCPP-MT is most likely due to the expanded lattice of GMPCPP-MT, in which the tubulin periodicity is expanded by 2-3% along the longitudinal axis compared to that of GDP-MT (Alushin *et al*., 2014). However, the different nucleotides in microtubules themselves (Estevez-Gallego et al., 2020) may also affect the affinity to D2. Therefore, we next investigated the affinity of D2 to other types of microtubules with expanded lattices. Taxol, a microtubule depolymerization inhibitor used as an anti-cancer drug, is known to expand microtubules and force microtubules to take a GMPCPP-bound-like structure (Yajima *et al*., 2012; Alushin *et al*., 2014; Kamimura *et al*., 2016). If the preference of D2 to GMPCPP-MT is attributed to the expanded lattice and not the interaction with the nucleotide itself, D2 should have a higher affinity for taxol-stabilized GDP-MT. To test this hypothesis, we conducted the same binding assay in the presence of 20 μM taxol, a concentration high enough to force microtubules to take the expanded lattice (Yajima *et al*., 2012).

Indeed, the presence of taxol increased D2-mCherry intensity on both GDP- and GMPCPP-MT, such that we could detect D2-binding on GDP-MT even at D2 concentrations as low as 100 nM (Fig. 2A). Quantification revealed that the intensity of D2-mCherry on GDP-MT increased from an undetectable level to 22 ± 6 a.u. at 250 nM D2, which is similar to the intensity of D2 bound to GMPCPP-MT without taxol (Fig. 2B). At 1 μM D2 with taxol, the amount of D2 bound to GDP-MT reached 85% that bound to GMPCPP-MT. This value remained constant (86%) when the D2 concentration was elevated to 4 μM, implying that the preference of D2-binding reached a plateau at 1 μM. These results support the idea that D2 distinguishes expanded/compact lattices, not the nucleotide state of microtubules.

We also tested the reversibility of the effects of taxol using a taxol-depletion assay (Fig. 2A). In this assay, microtubules were first equilibrated with a solution containing D2 and taxol, and then taxol was subsequently depleted by exchanging the solution to D2 solution without taxol. Considering the fast dissociation (k_{off} ~30 s^{-1}; Caplow *et al*.,1994) and the weak affinity (K_d ~2 μM; Li *et al*., 2000; Ross *et al*., 2004) of taxol with GDP-MT, no more than ~1% of the bound taxol could remain bound or rebind during the incubation in taxol-free buffer. The presence of a stoichiometric amount of taxol is needed to expand the lattice (Kamimura et al., 2016). Therefore, after the taxol depletion, a subset of GDP-MTs was expected to take the compact lattice. At 1 μM or higher concentrations of D2-mCherry, the D2-mCherry fluorescence intensity on the MTs did not change after the taxol depletion. However, at lower D2 concentrations, the behavior was different. Namely, at 100 nM D2, D2 molecules bound on the GDP-MT in the presence of taxol were completely dissociated after the taxol depletion. Consequently, the taxol depletion significantly decreased the D2 fluorescence intensity on GDP-MT to zero (4.0 ± 2.4 a.u. to -0.5 ± 1.1 a.u., Fig. 2B, Table 1). At 250 nM D2, the D2 dissociation by taxol-depletion was partial, but the intensity decrease was still significant (22 ± 6 a.u. to 17 ± 8 a.u., Fig. 2B, Table 1). In this condition, D2 occasionally remained on some subregions of GDP-MTs after taxol-depletion (Fig. 2C), so that the line profiles along the microtubules clearly showed a stepwise increase in mCherry intensity (Fig. 2D). The distinct amounts of residual D2 suggests that microtubules and/or D2 take distinct states in each subregion of GDP-MTs after taxol-depletion. Together, these results demonstrate that D2 recognizes the microtubule lattice expansion, and changes in the affinity between D2 and microtubules is reversible at low D2 concentrations.

D2 detects lattice expansion of native microtubules

TIRF microscopy showed that D2 affinity for microtubule positively correlates with the microtubule lattice expansion induced by GMPCPP or taxol. However, these chemical reagents do not exist in intact mammal cells. To confirm whether D2 can identify microtubule conformations in normal cells, we induced microtubule lattice expansion using a protein that is present in the cytoplasm. The microtubule motor protein KIF5C is known to trigger the transition of the GDP-MT lattice structure from the compacted to expanded state (Shima *et al*., 2018; Peet *et al*., 2018). Importantly, the microtubule lattice remains expanded for ~2 minutes after KIF5C dissociation is induced by a high ionic strength buffer (Shima *et al*., 2018), but it is immediately compacted (<4 seconds) when buffer containing ADP or AMPPNP is used instead (Peet *et al*., 2018, Shima *et al*., 2018). Therefore, KIF5C treatment and washout are useful for modulating the lattice structure of native GDP-MT.

We repeated the KIF5C pre-treatment assay with several concentrations of KIF5C and washout buffers while keeping the D2 concentration constant at 1 μM (Fig. 3A). Compared to the case without KIF5C pre-treatment, the D2-binding affinity to GDP-MT was significantly increased by pre-treatment with 0.1 μM KIF5C (Fig. 3B). Pre-treatment with higher concentrations of KIF5C further enhanced the D2 affinity for GDP-MT to almost the same level as that for GMPCPP-MT without the pre-treatment (Fig. 3B, C; Table 2). If D2 recognizes the lattice expansion induced by KIF5C, lattice compaction should lower the affinity between GDP-MT and D2 to the original weak state. Indeed, ADP-triggered lattice compaction upon KIF5C dissociation aborted D2-binding even at the highest KIF5C concentration tested (Fig. 3B, C). The mCherry intensity on GDP-MT did not drop to the original value ($p < 0.001$, Steel-Dwass test) but resembled the condition with 0.1 μM KIF5C pre-treatment. This incomplete rollback of the lattice structure may be due to the partial dissociation of D2, since ADP wash does not affect the binding of D2, which is a non-ATPase. To normalize the lattice structural deviation between conditions, we calculated the specificity of D2-binding by dividing the average mCherry intensity on GMPCPP-MT with that on GDP-MT (Fig. 3D). This analysis revealed that the specificity of D2 monotonically decreased in response to large amounts of KIF5C pre-treatment and restored the specificity to the original state after the ADP wash. This observation further supports the notion that D2-binding is sensitive to microtubule lattice spacing.

D2 expands the microtubule lattice, but the expansion is not meta-stable

Next, we speculated whether the "reader" ability of D2 contributes to expanding the lattice of GDP-MT when D2 excessively binds to it. To test this hypothesis, we conducted a microtubule expansion assay with a high concentration of D2 (Fig. 4A). We polymerized Cy5-labeled GDP-MT from Alexa Fluor 488-labeled GMPCPP seed and capped it with Alexa Fluor 488-labeled GMPCPP-MT to prevent depolymerization during the assay. Before adding D2, microtubules were straight along their entire length. With 4 μM D2, the microtubules were severely deformed despite extensive parallel flow during the buffer exchange (Fig. 4B). To precisely measure the microtubule length before and after D2-binding, we used a curve fitting algorithm on the fluorescence images. Microtubules were first fit to a two-dimensional (2D) B-spline Gaussian wall using the total fluorescence intensity. Subsequently, we measured the length of the Cy5-labeled region by a line scan of the Cy5 channel along the spline curve and fitting to the error function at both ends (see Methods). The presence of D2 caused a longitudinal elongation of GDP-MT that was associated with the lattice expansion. 4 μM D2 induced a 3.2 ± 0.8% (mean ± S.D.) lattice expansion, which is comparable to TPX2/GMPCPP-induced double expansion (Zhang *et al*., 2018), the most expanded state reported (LaFrance *et al*., 2022). Moreover, the addition of the CKK domain to the D2 construct decreased the expansion rate to 0.9 ± 1.2% (mean ± S.D., Fig. S2), even though D2-CKK showed almost the same binding distribution along microtubules as D2 at this concentration (Fig. S2C, D). These results suggest that D2, not CKK, primarily leads the lattice expansion.

As mentioned above, the lattice expansion induced by KIF5C lasts for ~2 min even after KIF5C dissociation by a high ionic strength buffer. Therefore, the KIF5C-triggered expanded lattice is assumed to be a meta-stable state (Shima *et al*., 2018). Since D2 expanded the lattice more than KIF5C did, the D2-induced expansion may last longer than that induced by KIF5C. To check the meta-stability of the D2-induced expanded lattice, D2 was

washed out with the high ionic strength buffer after the lattice expansion, and the microtubule length was measured. Contrary to our expectation, the lattice compaction was completed within 90 seconds after the D2 dissociation (Fig. 4C). The results of the taxol-depletion assay (Fig. 2), in which D2 dissociated from a subset of the microtubule region immediately after taxol removal, also support the notion that insufficient amounts of bound D2 cause an immediate return of the expanded lattice to the compact state. Note that in the KIF5C pre-treatment assay (Fig. 3), the enhanced D2 affinity remained after KIF5C dissociation by the same buffer. Therefore, the lattice expansion triggered by D2 is reminiscent of that by KIF5C, but their effects are different in terms of stability against the compaction. Finally, we confirmed no microtubule length dependency on the expansion and returning events (Fig. 4D). Collectively, our expansion assay revealed that D2 can convert the microtubule lattice into the expanded state, but the D2-triggered expanded state is not meta-stable, so it returns to the compacted state immediately after the dissociation of D2.

D2-triggered expanded lattice is resistant to microtubule depolymerization

We revealed that D2-binding transforms microtubules to the expanded state. Although many types of microtubules with the expanded lattice are resistant to depolymerization, it is unclear if this is true for D2-induction. Therefore, we quantified the depolymerization rate by glycerol depletion with or without 4 μM D2 (Fig. 5A). A comparison of time lapse images in the absence (Fig. 5B) and presence of D2 (Fig. 5C) clearly indicated that depolymerization was strongly suppressed by 4 μM D2. Representative kymographs also showed an obvious difference between the two conditions (Fig. 5D, E). Before quantifying the depolymerization rate, we could not build kymographs for most microtubules, since microtubules changed their curves during depolymerization. As a workaround, we derived the depolymerization rate from the total fluorescence intensity in each specific region that surrounds individual microtubules throughout the imaging time (Fig. S3). We found that microtubule depolymerization dramatically slowed down from 0.82 ± 0.30 μm s^{-1} (mean ± S.D.) to 0.046 ± 0.028 μm s^{-1} upon exposure to 4 μM D2 (Fig. 5F). We also investigated if D2 accumulates at the depolymerizing microtubule tips like MAPs such as Ska1 complex (Schmidt *et al.*, 2012), since tip accumulation will expand microtubules more and effectively prevent further depolymerization. However, we found no D2 localization, as no intensity peaks were detected in the averaged line scans (Fig. S4). These experiments suggest that the lattice expansion by D2 protects microtubules from depolymerization.

4. Discussion

In this study, we demonstrated that the D2 region of human CAMSAP3 preferentially binds to the expanded lattice of microtubules. At saturating levels, D2 expanded the microtubule lattice by 3.2% (Fig. 4), which slowed the microtubule depolymerization rate down ~18 fold (Fig. 5). Combining these results with previously known functions of the CKK domain, we suggest a detailed model of microtubule stabilization by CAMSAP3 (Fig. 6A). The interaction between microtubules and CAMSAP3 is first formed via the CKK domain, since it occurs regardless of the presence of other CAMSAP3 domains (Jiang *et al*., 2014). Because D2 alone does not track either end of dynamic microtubules (Atherton *et al*., 2017), this CKK binding is likely needed for D2 to bind at the minus end of microtubules. Once a CAMSAP3 protein is bound to the microtubule surface, the local concentration of the D2 region at the minus end is dramatically increased. Assuming that the peptide between the microtubule binding region of D2 and the CKK domain (residues 1023-1111 for human CAMSAP3) takes the disordered conformation, which is predicted by AlphaFold2, and the inter-residue distance is 0.4 nm (Ainavarapu *et al.*, 2007), a D2 molecule is confined to a volume of $4/3 \times \pi \times (0.4 \times 88)^3 = 9.1 \times 10^4$ nm^3 after CKK binding; thus, the D2 local concentration is estimated to be over 20 μM. Note that the local concentration is likely underestimated, since the peptide chain is unlikely to be tautly stretched due to entropic energy loss. Considering 4 μM D2 was sufficient to expand the lattice of GDP-MT (Fig. 4B), a local concentration over 20 μM should be high enough to convert the minus end into the expanded state with high affinity for D2. As a result, CAMSAP3 protein strongly interacts with the minus end of microtubules via divalent interactions of the CKK domain and D2 region. At the same time, the minus end is stabilized by the D2-induced lattice expansion (Fig. 5F). This expanded lattice recruits more CAMSAP3 molecules by promoting D2-microtubule interactions and prevents the dissociation of CAMSAP3. Previous work using recombinant CAMSAPs also supports the importance of non-CKK domains on the enhancement of minus-end affinity (Hendershott *et al.*, 2014). Newly polymerized microtubule minus ends should interact with other CAMSAP3 molecules in the cytoplasm via the CKK domain, resulting in microtubules near the minus end decorated with CAMSAP3 over a long range (Jiang *et al*., 2014).

This model is consistent with the correlation between the domain composition of vertebrate CAMSAPs and their ability to decorate and stabilize microtubules. Previous truncation studies have shown that the D2 domain of CAMSAP3 and MBD in CAMSAP2/3 preferentially bind to GMPCPP-MT over GDP-MT, implying that these regions recognize the expanded lattice (Jiang *et al.*, 2014; Atherton *et al.*, 2017). Similar to the number of regions showing this preference, the microtubule stabilizing effect is higher for CAMSAP3 than CAMSAP2. Also, our model can explain why CAMSAP1, which does not have any region with a high affinity for the expanded lattice, barely affects microtubule stability (Fig. 6B). Thus, the number of regions that prefer the expanded lattice is apparently proportional to the microtubule stabilization effect (Jiang *et al*., 2014; Hendershott *et al*., 2014). In this study, we focus on the D2 region of CAMSAP3 due to difficulty in expressing MBD in soluble fractions in our system. Future analysis of MBD together with mutational and swapping analyses of these regions will strengthen our model and provide a comprehensive understanding of the roles of MBD and D2.

Overall, we demonstrated that the D2 region of CAMSAP3 has two functions: to identify the expanded microtubule lattice (Fig. 1–3) and to expand the compact lattice of GDP-MT (Fig. 4, 5). Both of these functions are common with the motor protein KIF5C and mitosis regulator TPX2. If we assume that the "reading" and "writing" codes on the lattice are correlated, there is a trade-off between the binding specificity of the proteins and their effectiveness at expanding the lattice. If the specificity is low (low reading ability), like in the case of KIF5C, the protein can spontaneously bind to the compacted lattice well, but the resulting expansion is small (low writing ability). Indeed, KIF5C expands the lattice by only ~1% (Shima *et al*., 2018; Peet *et al*., 2018), whereas D2 expands it by ~3% (Fig. 4C). On the contrary, proteins with high specificity, like TPX2 and D2, are expected to expand the lattice longer (high writing ability) but do not bind well on a compact lattice because of the higher specificity for the expanded condition. Therefore, these highly specific proteins require another mechanism to recruit proteins on a compacted lattice before the expansion occurs. As for TPX2, recent light and electron microscopy studies have shown that it is locally concentrated on microtubules by liquid-liquid phase separation and Rayleigh instability (King and Petry, 2020; Setru *et al.*, 2021). As for D2, the CKK domain in the same CAMSAP3 molecule is most likely concentrated at the microtubule minus end (Fig. 6A). Thus, the "reading" and "writing" abilities of these proteins may have been evolutionarily optimized according to their protein structure, binding partners, and cellular distribution and function.

Having both "reading" and "writing" ability can produce positive feedback between the binding affinity and the lattice structure of microtubules, resulting in the cooperative binding/dissociation of MAPs. KIF5C, for instance, shows cooperative binding on GDP-MTs so that it accumulates in a subset of GDP-MTs, while other subsets bound to very few KIF5C molecules (Shima *et al*., 2018). D2 demonstrated similar cooperativity in our taxol-depletion assay. At 250 nM D2 after taxol-depletion, GDP-MTs showed two distinct types of affinity to D2: subregions where many D2 remained bound and where most D2 are dissociated (Figure 2C, 2D). Due to the similarity with KIF5C, we assume that this cooperative dissociation of D2 is a consequence of the positive feedback of D2 dissociation and lattice compaction. When a number of D2 molecules exceeding a threshold stochastically dissociated from a certain subregion of GDP-MTs, the lattice of the subregion should return to the compacted form, which lowers the affinity to D2, resulting in further D2 dissociation. Since microtubule lattice spacing is interconnected with adjacent tubulin dimers, tubulin dimers in a certain region of microtubules are likely to have similar lattice spacing as observed in Fig. 2C. However, the cooperativity of D2 binding/dissociation was only seen in a specific condition. Thus, the positive feedback between the binding affinity and the lattice structure is likely less in the case of D2 compared with other MAPs that have "reading" and "writing" abilities.

Under low concentrations of D2 (100 nM and 250 nM), the D2 intensity on GMPCPP-MTs and GDP-MTs significantly changed after taxol depletion (Fig. 2B). In all cases except on GMPCPP-MTs at 250 nM D2, the D2 intensity was decreased by taxol depletion. These results are consistent with taxol depletion reversibly changing the MT lattice into a compacted form, which decreases the affinity with D2. However, in the case of GMPCPP-MTs at 250 nM D2, the D2 intensity increased by ~16% after taxol depletion (Table 1). This effect may be due to the increase in total D2 concentration. In our assays, taxol was depleted by introducing D2 solution without taxol. Therefore, because of remaining D2 molecules on microtubules, the total D2

concentration in the chamber may be higher than 250 nM after taxol-depletion. This situation is also true for other concentrations, but the strength of the effect depends on the amount of remaining D2 on microtubules. At 250 nM D2, D2 showed frequent binding on GMPCPP-MTs but not on GDP-MTs in the absence of taxol (Figure 1C,1D); thus, more D2 should remain bound on GMPCPP-MTs than on GDP-MTs after taxol depletion. Therefore, the effect of taxol-depletion can be explained by the competing effects of residual D2 and changes in the lattice structure. These competing effects are insignificant when most of the binding sites on MTs are occupied by D2, which corresponds to fewer binding sites and an expanded lattice, as shown in assays using higher D2 concentrations (Figure 2, 1 μM and 4 μM).

It is worth noting that the microtubule structure is more complex than just an expanded or compact lattice. Contrary to KIF5C-binding, the lattice expansion triggered by D2-binding was not meta-stable, returning to the original status immediately after D2 dissociation (Fig. 4C). Notably, KIF5C-induced expansion lasts longer even though the relative expansion rate is less than that induced by D2, highlighting the differences in KIF5C- and D2-induced expanded lattices. There is also an inconsistency in that D2 binding GMPCPP-MT was enhanced by KIF5C pre-treatment (Fig. 3) even though KIF5C does not expand the lattice of GMPCPP-MT further (Shima *et al*., 2018). Also, even though the GTP-cap of microtubules is considered to have an expanded lattice structure (Zhang *et al*., 2018), one study showed that D2 does not track either end of dynamic microtubules, suggesting that D2 does not prefer the lattice of the GTP-cap (Atherton *et al*, 2017). Future structural studies on D2-coated microtubules and comparisons with the structure of KIF5C-bound GDP-MT (Shima *et al*., 2018) or the GTP-cap of dynamic microtubules will reveal the structural diversity of microtubules with expanded lattices and explain what causes these differences.

Materials and Methods

1. Protein purification and labeling

Tubulin was purified from porcine brains by polymerization/depolymerization cycles in high molarity buffer as described previously (Castoldi and Popov, 2003). For GTP-bound tubulin, polymerization/depolymerization was repeated for three cycles. In the final cycle, tubulin was depolymerized in PEM (100 mM PIPES-KOH, 1 mM EGTA, and 2 mM $MgSO_4$, pH 6.9 supplemented with 0.1 mM GTP, snap-frozen and stored in liquid nitrogen. To prepare GMPCPP-bound tubulin, two cycles were conducted in the same way as GTP-bound tubulin, and purified tubulin was subsequently subjected to two polymerization/depolymerization cycles using 0.1 mM GMPCPP (NU-405L; Jena Bioscience) instead of 1 mM GTP. In the final cycle, tubulin was depolymerized in PEM containing 0.1 mM GMPCPP and stored in the same way as GTP-bound tubulin.

Fluorescently labeled tubulin and biotinylated tubulin were prepared by adding Alexa Fluor 488 NHS ester (A20000; Thermo Fisher), Sulfo-Cy5 NHS Ester (13320; Lumiprobe) or Sulfo-Cy5 NHS Ester (13320; Lumiprobe) dissolved in DMSO to polymerize microtubules. Unreacted labels were removed by two dilutions and ultracentrifugation of the microtubules. Labeled tubulin samples were mixed with intact tubulin at the indicated labeling rates, snap-frozen and stored in liquid nitrogen.

The human CAMSAP3 gene was bought from Riken (GNP Clone IRAL050D13) and cloned into pET11a plasmid vector. Plasmids were transformed into Rosetta II competent cells (71397; Novagen) and incubated in 2x YT medium (16 g/L bacto-tryptone, 10 g/L yeast extract, 5 g/L NaCl) supplemented with 10 µg/mL ampicillin in a 37°C shaker until the OD600 reached ~0.6. Protein expression was induced by a 5.5-hour incubation at 18°C in the presence of 0.5 mM IPTG. Bacteria were collected, snap-frozen in liquid nitrogen and stored at -80°C. For protein purification, bacteria pellets were resuspended in lysis buffer (50 mM Tris-HCl, 500 mM NaCl, 10 mM imidazole, pH 8.0) supplemented with protease inhibitor cocktail (1 mM 4-(2-aminoethyl) benzenesulfonil fluoride, 20 µM Leupeptin, 8.7 µM Pepstatin, and 1 mM N-p-tosyl-L-argininie-methyl ester), sonicated and pelleted by centrifugation at 18,000 x g for 10 min. D2-mCherry was retrieved from the supernatant using its 6x Histidine tag by Ni-NTA agarose resin (141-09764; FUJIFILM). The resin was washed twice with 1.5 column volumes of wash buffer A (50 mM Tris-HCl, 500 mM NaCl, 100 mM imidazole, pH 8.0), twice with 1.5 column volumes of wash buffer B (50 mM Tris-HCl, 500 mM NaCl, 150 mM imidazole, pH 8.0) and lastly once with wash buffer C (50 mM Tris-HCl, 500 mM NaCl, 300 mM imidazole, pH 8.0). The second fraction from the washout using wash buffer B was concentrated and mixed with BRB30 (30 mM PIPES-KOH, 1 mM EGTA, 2mM $MgSO_4$, pH 7.0) using a 30-kDa-cutoff centrifugal filter (UFC503096; Merck). Finally, D2-mCherry solution was snap-frozen with liquid nitrogen and stored at -80°C.

KIF5C (residues 1–411) was purified from the *E coli* recombinant protein purification system. Mouse KIF5C gene was cloned into pET11a plasmid with 6xHis-tag inserted in the N-terminal end. Plasmids were first transformed into Rosseta II competent cells and incubated in 2x YT medium supplemented with 10 µg/mL ampicillin and 10 µg/mL Chloramphenicol in a 37°C shaker until the OD600 reached 0.36. Protein expression was induced by a 14-hour incubation at 18°C in the presence of 0.25 mM IPTG. Bacteria were resuspended in lysis buffer (PEM, 150 mM NaCl, 10 mM imidazole, pH 6.9, supplemented with protease inhibitor cocktail), sonicated and pelleted by centrifugation. KIF5C was incubated with Ni-NTA agarose resin and washed with

391 1.5 column volumes of wash buffer A (PEM, 150 mM NaCl, 100 mM imidazole, pH 6.9) and twice with 1.5
392 column volumes of wash buffer B (PEM, 150 mM NaCl, 150 mM imidazole, pH 6.9). KIF5C was eluted from
393 the resin with elution buffer (PEM, 150 mM NaCl, 300 mM imidazole, pH 6.9). The elution fraction was
394 concentrated and buffer-exchanged to BRB80 buffer (80 mM PIPES-KOH, 1 mM EGTA, 2 mM $MgSO_4$, pH
395 7.3) supplemented with 8% glycerol and 0.5 mM DTT using a 30-kDa-cutoff centrifugal filter (UFC503096;
396 Merck). Finally, KIF5C solution was snap-frozen with liquid nitrogen and stored at -80°C.
397
398 2. Preparation for binding assay
399 A PEG-biotin-coated glass chamber was made by silane coupling and a succinimidyl ester reaction. Cover
400 glasses (C022221S; Matsunami Glass) were first subjected to sonication in 1 N KOH and plasma treatment.
401 Glass surfaces were coated with an amino group by sandwiching N-2-(aminoethyl)-3-aminopropyl-
402 triethoxysilane (KBE-603; Shin-Etsu Chemical) and incubation for 20 min at room temperature. These glasses
403 were washed with deionized water 20 times and then incubated with 200 mg/mL of 0.5%-biotinylated NHS-
404 PEG (ME-050-TS and BI-050-TS; NOF) for 90 min at room temperature. Coated glasses were stuck to each
405 other with 30-µm double-sided tape (5603; Nitto-Denko) to make an ~2-mm wide flowing chamber. The glasses
406 were sealed in a food saver in vacuo and stored at -80°C until use.
407 GMPCPP-bound tubulin labeled with Alexa Fluor 488 (2% labeled) and biotin (5% labeled) was incubated
408 at 27°C for 1 h to promote nucleation, followed by 1 h of polymerization at 37°C. Polymerized microtubule
409 samples were purified by centrifugation at 20,000 x g, 35°C for 25 min.
410 The glass chamber was treated as follows. First, 1 mg/mL NeutrAvidin was loaded into the chamber and
411 incubated for 2 min to let it bind to biotin molecules covalently connected to the glass surface. The glass surface
412 was subsequently deactivated by adding and incubating with 10x blocking solution (1 mg/mL casein, 1%
413 Pluronic F127) for 2 min. After washing them out with BRB80 containing 25% glycerol, GMPCPP-MT seeds
414 were loaded into the chamber and incubated for 2 min to immobilize microtubules on the glass surface. Unbound
415 microtubules were washed out with BRB80 containing 10x blocking solution and 1 mM GTP. To polymerize
416 GDP-MT from the seeds, 28 µM Cy5-labeled tubulin (labeling rate 2%) in polymerization buffer (BRB80, 2x
417 blocking solution, 1 mM GTP) was applied to the chamber, polymerized for 5 min and terminated by washing
418 free tubulin out with washout buffer (BRB80, 25% glycerol, 2x blocking solution). To completely hydrolyze
419 GTP, the chamber was incubated for more than 30 min before any subsequent experiments.
420
421 3. Imaging
422 Images of *in vitro* assays were acquired using an Eclipse Ti (Nikon) TIRF microscope. The microscope was
423 equipped with a 488 nm laser (Coherent OBIS488-60LS), a 532 nm laser (Coherent OBIS532-20LS), a 640 nm
424 laser (Coherent CUBE640-40), a FF01-390/482/532/640-25 excitation filter (Semrock), a Di01-
425 R405/488/532/635-25x36 dichroic mirror (Opto-line), a FF01-446/510/581/703-25 fluorescence filter (Opto-
426 line), an Apo TIRF 60x/1.49 oil objective lens (Nikon) and a Sona sCMOS camera (Andor). All image
427 acquisitions were managed with Micro-manager (v2.0.0; Edelstein *et al.*, 2014). Imaging was performed at room
428 temperature (23-26°C).

429
430 4. Binding assay
431 D2-mCherry in imaging buffer (BRB80, 25% glycerol 1x blocking solution, 0.1% methylcellulose, 5 mM
432 protocatechuic acid (Pacific Bioscience), 5 mM TSY (Pacific Bioscience), and 50 nM protocatechuate-3,4-
433 dioxygenase (Pacific Bioscience)) was applied to the microtubule-immobilized glass chamber (see 2.
434 Preparation for binding assay). After 5 min of incubation, image acquisition was conducted for all registered
435 positions. To increase the signal-to-noise ratio, five frames were taken for every position and channel.
436 For assays in the presence of taxol, D2-mCherry in imaging buffer was supplemented with 20 μM taxol,
437 and images were acquired the same way. Taxol depletion was conducted by exchanging the solution with a
438 sample of same D2 concentration without taxol. Images were taken after a 5-minute incubation.
439 Since the binding activity of D2 was lost quickly after being thawed (< 1 hour), we prepared new samples
440 every 30 min.
441
442 5. Binding assay with KIF5C pre-treatment
443 During this experiment, 1 μM D2-mCherry in imaging buffer was used for the D2-mCherry samples, and
444 variable concentrations of KIF5C in BRB30 with 25% glycerol were used for the KIF5C pre-treatment. A
445 microtubule-immobilized glass chamber (see 2. Preparation for binding assay) was first incubated with D2-
446 mCherry for 5 min. As a no-pre-treatment control, microtubule-bound D2 was dissociated by a 1-min incubation
447 in high-salt buffer (7.5x PEM, 25% glycerol) followed by washout with BRB80 containing 25% glycerol. Again,
448 D2-mCherry was applied, and the chamber was incubated for 5 min before the image acquisition.
449 For 0.1, 0.5 and 2.0 μM KIF5C pre-treatment, the incubation/dissociation cycle described below was
450 repeated in the same chamber following the previous image acquisition of D2-bound microtubules. First, D2
451 was dissociated and washed out by a 1-min incubation in high-salt buffer and a 30-second incubation in BRB80
452 containing 25% glycerol. Microtubules were subsequently expanded by the addition of KIF5C and incubated
453 for 1 min. Next, KIF5C was dissociated and washed out by a 1-min incubation in high-salt buffer and 30-s
454 incubation in BRB80 containing 25% glycerol. Finally, D2 was applied and incubated for 5 min before the
455 image acquisition.
456 For the compaction experiment, pre-treatment with 2.0 μM KIF5C was repeated as above except the buffer
457 used for the KIF5C dissociation was ADP buffer (BRB80, 25% glycerol, 1 mM ADP) and not a high-salt buffer.
458 Note that since this assay takes ~1 h for each run, new D2 samples were prepared between 0 μM and 0.1
459 μM pre-treatments in addition to the 0.5 μM and 2.0 μM pre-treatments.
460
461 6. Data analysis of binding assays
462 Images acquired by TIRF microscopy were exported as OME-TIF files. Image processing and analysis were
463 done using Python (v3.9.7).
464 To correct for uneven irradiation by the laser, images were first processed using custom site-package impy
465 (https://github.com/hanjinliu/impy; v2.1.1) as follows. For each channel, all acquired 4D image stacks (stage
466 position, time frame and XY) were projected along the axes of stage positions and frames by the median to

create a 2D background image. This background image was fit to a 2D diagonal Gaussian function:

$$I_{BG}(x,y) = I_0 \exp\left[-(x-\mu_x)^2/2\sigma_x^2 - \left(y-\mu_y\right)^2/2\sigma_y^2\right] + C$$

where I_0 is the peak background intensity, μ_x and μ_y are the peak positions, σ_x and σ_y are the variations of the Gaussian function, and C is a constant. Subsequently, for each separate image slice, intensity values $I(x,y)$ were corrected by:

$$I'(x,y) = I(x,y)/I_{BG}(x,y) \cdot \max(I_{BG}) - \max(I_{BG})$$

to extract the true fluorescence intensity. The corrected image $I'(x,y)$ was averaged by the second to fifth frames and saved as 32-bit floating image stacks in TIF format. The first frame was not used for the analysis because some of them were not in-focus due to the short buffering time after the stage movement.

To remove leakage of the fluorescence intensity between channels, blue-to-green, green-to-blue, red-to-green and green-to-red leakage ratios were determined as follows. The green channel mean intensity along Alexa Fluor 488-labeled microtubules and Cy5-labeled microtubules were measured without D2-mCherry to calculate the blue-to-green and red-to-green leakage. Microtubules saturated with D2 (microtubules equilibrated with 4 μM D2 and 20 μM taxol) were used to measure the blue channel mean intensity along Cy5-labeled microtubules and red channel mean intensity along Alexa Fluor 488-labeled microtubules to calculate green-to-blue and green-to-red leakage. Leakage-corrected images were saved as 32-bit floating image stacks in TIF format.

Average fluorescence intensities along microtubules were quantified using Python image viewer napari (v0.4.16; Sofroniew *et al.*, 2022) and custom plugin napari-filaments (https://github.com/hanjinliu/napari-filaments; v0.2.1). Briefly, fluorescence intensities (Alexa Fluor 488 channel or Cy5 channel) of the non-overlapping regions of microtubules were manually selected and fit to 2D spline curves. For the spline of length L, $\lfloor L \rfloor + 1$ sample points were placed at equal intervals including the edges (i.e., placed for every ~1 pixel), and the intensities were interpolated by cubic interpolation. Average fluorescence intensities were calculated as the average of all interpolated intensities. All statistical tests were calculated using scipy (v1.7.3), statsmodel (v0.13.2; Seabold and Perktold, 2010) or scikit-posthocs (v0.7.0; Terpilowski, 2019).

7. Microtubule expansion assay

Microtubule immobilization was carried out similar to the binding assay (see 4. Binding assay) but slightly modified to fit the expansion assay. After GMPCPP-MT was added, 28 μM Cy5-labeled tubulin (10% labeled) was used for a 15-min polymerization period to lengthen and brighten the microtubules. Subsequently, 8 μM Alexa Fluor 488-labeled tubulin (2% labeled) with 1 mM GMPCPP was loaded into the chamber and polymerized for 20 minutes. Polymerization was terminated by washing free tubulin out with washout buffer. Images were acquired before and after 4 μM D2-mCherry in imaging buffer was added to the chamber followed by the dissociation of D2 by a 1-min incubation in high-salt buffer and washout by imaging buffer for 30 s.

To calculate expansion, a background correction was performed in the same way as the data analysis for the binding assay (see 6. Data analysis of binding assays). Microtubule lengths were measured using napari-filaments as follows (Fig. S5). First, the Cy5 channel and Alexa Fluor 488 channel of the image were added with 1:1 weight to create a total intensity image. This image was used for 2D spline fitting as mentioned in the

data analysis of the binding assay (see 6. Data analysis of binding assays). Next, the spline curves were clipped at the Cy5-labeled microtubule edges by fitting to the error function:

$$f(x) = \frac{a-b}{2}\left(1 + \mathrm{erf}\left(\frac{x - x_0}{\sqrt{2}\sigma}\right)\right) + b \qquad \left(\mathrm{erf}(x) = \frac{2}{\sqrt{\pi}}\int_0^x e^{-t^2}\,dt\right)$$

The parameters of the error function indicate that intensity increases from b to a, where the inflection point of the intensity change is x_0. Cy5-labeled microtubule lengths were obtained by fragmenting the spline curve into 1024 pieces and summing the lengths of all fragments.

8. Microtubule depolymerization assay

Cy5-labeled GDP-MT (10% labeled) was grown from Alexa Fluor 488-labeled GMPCPP-MT (2% labeled) in the same way as the microtubule expansion assay (see 7. Microtubule expansion assay). After a 30-min incubation to hydrolyze GTP completely, the chamber was washed with washout buffer (BRB80, 25% glycerol, 2x blocking solution) with or without 4 μM D2 and incubated for 5 min. Subsequently, glycerol-free imaging buffer (BRB80, 1x blocking solution, 0.1% methylcellulose, 5 mM protocatechuic acid, 5 mM TSY, and 50 nM protocatechuate-3,4-dioxygenase) with or without 4 μM D2 was flowed into the chamber, and the image acquisition was started immediately. For experiments without D2, images were taken at 0.5-s intervals; for those with D2, images were taken at 5-s intervals. Signals from the mCherry channel were also taken for the experiments in Fig. S4.

Instead of building kymographs, we measured the decrease in Cy5 total intensity to quantify the depolymerization rate. Areas that microtubules occupied during depolymerization were manually drawn using max projection as the reference. The total Cy5 intensity in the area was measured for every frame, and the values were converted into length using the ratio of the microtubule length to total Cy5 intensity of the first frame. The depolymerization rate was determined by a linear regression of data points that corresponded to microtubule lengths longer than 0.5 μm using the scikit-learn package (v1.0.1; Pedregosa *et al*., 2011). This workflow was applied to all microtubules independently.

Data availability

Image data sets and Python scripts are available at https://zenodo.org/record/7634450.

Acknowledgement

This work is supported by JSPS KAKENHI (18K06147,19H05379 and 21H00387 to T.S.).

We thank P. Karagiannis (Sofia Science Writing) for proofreading and helpful comments on the manuscript.

We also thank the members of the Uemura laboratory for valuable discussions.

Author contributions

Conceptualization, H.L. and T.S.; Data curation, H.L.; Methodology, H.L. and T.S.; Investigation, H.L.; Analysis, H.L.; Supervision, T.S.; Visualization, H.L.; Writing – original draft, H.L.; Writing – review & editing, H.L. and T.S.

Conflict of interests

The authors declare no conflicts of interest associated with this manuscript.

References

Aher A, Kok M, Sharma A, Rai A, Olieric N, Rodriguez-Garcia R, Katrukha EA, Weinert T, Olieric V, Kapitein LC, *et al.* (2018) CLASP suppresses microtubule catastrophes through a single TOG domain. *Developmental Cell* 46:40–58

Ainavarapu SRK, Brujić J, Huang HH, Wiita AP, Lu H, Li L, Walther KA, Carrion-Vazquez M, Li H, Fernandez JM (2007) Contour length and refolding rate of a small protein controlled by engineered disulfide bonds. *Biophysical Journal* 92:225–233

Akhmanova A, Steinmetz MO (2019) Microtubule minus-end regulation at a glance. *Journal of Cell Science* 132:jcs227850

Alushin GM, Lander GC, Kellogg EH, Zhang R, Baker D, Nogales E (2014) High-resolution microtubule structures reveal the structural transitions in αβ-tubulin upon GTP hydrolysis. *Cell* 157:1117–1129

Atherton J, Jiang K, Stangier MM, Luo Y, Hua S, Houben K, Van Hooff JJ, Joseph A-P, Scarabelli G, Grant BJ, *et al.* (2017) A structural model for microtubule minus-end recognition and protection by CAMSAP proteins. *Nature Structural & Molecular Biology* 24:931–943

Atherton J, Luo Y, Xiang S, Yang C, Rai A, Jiang K, Stangier M, Vemu A, Cook AD, Wang S, *et al.* (2019) Structural determinants of microtubule minus end preference in CAMSAP CKK domains. *Nature Communications* 10:5236

Ayukawa R, Iwata S, Imai H, Kamimura S, Hayashi M, Ngo KX, Minoura I, Uchimura S, Makino T, Shirouzu M, *et al.* (2021) GTP-dependent formation of straight tubulin oligomers leads to microtubule nucleation. *Journal of Cell Biology* 220

Caplow M, Shanks J, Ruhlen R (1994) How taxol modulates microtubule disassembly. *Journal of Biological Chemistry* 269:23399–23402

Castoldi M, Popov AV (2003) Purification of brain tubulin through two cycles of polymerization–depolymerization in a high-molarity buffer. *Protein Expression and Purification* 32:83–88

Coquand L, Victoria GS, Tata A, Carpentieri JA, Brault J-B, Guimiot F, Fraisier V, Baffet AD (2021) CAMSAPs organize an acentrosomal microtubule network from basal varicosities in radial glial cells. *Journal of Cell Biology* 220:e202003151

Dent EW, Baas PW (2014) Microtubules in neurons as information carriers. *Journal of Neurochemistry* 129:235–239

Dogterom M, Koenderink GH (2019) Actin–microtubule crosstalk in cell biology. *Nature Reviews Molecular Cell Biology* 20:38–54

Edelstein AD, Tsuchida MA, Amodaj N, Pinkard H, Vale RD, Stuurman N (2014) Advanced methods of microscope control using μManager software. *Journal of Biological Methods* 1

Estévez-Gallego J, Josa-Prado F, Ku S, Buey RM, Balaguer FA, Prota AE, Lucena-Agell D, Kamma-Lorger C, Yagi T, Iwamoto H, *et al.* (2020) Structural model for differential cap maturation at growing microtubule ends. *Elife* 9:e50155

Farmer V, Arpağ G, Hall SL, Zanic M (2021) XMAP215 promotes microtubule catastrophe by disrupting the growing microtubule end. *Journal of Cell Biology* 220:e202012144

Feng C, Thyagarajan P, Shorey M, Seebold DY, Weiner AT, Albertson RM, Rao KS, Sagasti A, Goetschius DJ, Rolls MM (2019) Patronin-mediated minus end growth is required for dendritic microtubule polarity. *Journal of Cell Biology* 218:2309–2328

Gadde S, Heald R (2004) Mechanisms and molecules of the mitotic spindle. *Current Biology* 14:R797–R805

Goodson HV, Jonasson EM (2018) Microtubules and microtubule-associated proteins. *Cold Spring Harbor Perspectives in Biology* 10:a022608

Goodwin SS, Vale RD (2010) Patronin regulates the microtubule network by protecting microtubule minus ends. *Cell* 143:263–274

Hendershott MC, Vale RD (2014) Regulation of microtubule minus-end dynamics by CAMSAPs and Patronin. *Proceedings of the National Academy of Sciences* 111:5860–5865

Hyman AA, Chrétien D, Arnal I, Wade RH (1995) Structural changes accompanying GTP hydrolysis in microtubules: information from a slowly hydrolyzable analogue guanylyl-(alpha, beta)-methylene-diphosphonate. *The Journal of Cell Biology* 128:117–125

Imasaki T, Kikkawa S, Niwa S, Saijo-Hamano Y, Shigematsu H, Aoyama K, Mitsuoka K, Shimizu T, Aoki M, Sakamoto A, *et al.* (2022) CAMSAP2 organizes a γ-tubulin-independent microtubule nucleation centre through phase separation. *Elife* 11:e77365

Jiang K, Hua S, Mohan R, Grigoriev I, Yau KW, Liu Q, Katrukha EA, Altelaar AM, Heck AJ, Hoogenraad CC, *et al.* (2014) Microtubule minus-end stabilization by polymerization-driven CAMSAP deposition. *Developmental Cell* 28:295–309

Job D, Valiron O, Oakley B (2003) Microtubule nucleation. *Current Opinion in Cell Biology* 15:111–117

Kamimura S, Fujita Y, Wada Y, Yagi T, Iwamoto H (2016) X-ray fiber diffraction analysis shows dynamic changes in axial tubulin repeats in native microtubules depending on paclitaxel content, temperature and GTP-hydrolysis. *Cytoskeleton* 73:131–144

King MR, Petry S (2020) Phase separation of TPX2 enhances and spatially coordinates microtubule nucleation. *Nature Communications* 11:270

LaFrance BJ, Roostalu J, Henkin G, Greber BJ, Zhang R, Normanno D, McCollum CO, Surrey T, Nogales E (2022) Structural transitions in the GTP cap visualized by cryo-electron microscopy of catalytically inactive microtubules. *Proceedings of the National Academy of Sciences* 119:e2114994119

Li Y, Edsall R, Jagtap PG, Kingston DG, Bane S (2000) Equilibrium studies of a fluorescent paclitaxel derivative binding to microtubules. *Biochemistry* 39:616–623

Meng W, Mushika Y, Ichii T, Takeichi M (2008) Anchorage of microtubule minus ends to adherens junctions regulates epithelial cell-cell contacts. *Cell* 135:948–959

Mitchison T, Kirschner M (1984) Dynamic instability of microtubule growth. *Nature* 312:237–242

Morikawa M, Yajima H, Nitta R, Inoue S, Ogura T, Sato C, Hirokawa N (2015) X-ray and Cryo-EM structures reveal mutual conformational changes of Kinesin and GTP-state microtubules upon binding. *The EMBO Journal* 34:1270–1286

Nakata T, Niwa S, Okada Y, Perez F, Hirokawa N (2011) Preferential binding of a kinesin-1 motor to GTP-tubulin–rich microtubules underlies polarized vesicle transport. *Journal of Cell Biology* 194:245–255

Pedregosa F, Varoquaux G, Gramfort A, Michel V, Thirion B, Grisel O, Blondel M, Prettenhofer P, Weiss R, Dubourg V, *et al.* (2011) Scikit-learn: Machine learning in Python. *The Journal of Machine Learning Research* 12:2825–2830

Peet DR, Burroughs NJ, Cross RA (2018) Kinesin expands and stabilizes the GDP-microtubule lattice. *Nature Nanotechnology* 13:386–391

Pongrakhananon V, Saito H, Hiver S, Abe T, Shioi G, Meng W, Takeichi M (2018) CAMSAP3 maintains neuronal polarity through regulation of microtubule stability. *Proceedings of the National Academy of Sciences* 115:9750–9755

Roostalu J, Cade NI, Surrey T (2015) Complementary activities of TPX2 and chTOG constitute an efficient importin-regulated microtubule nucleation module. *Nature Cell Biology* 17:1422–1434

Ross JL, Santangelo CD, Makrides V, Fygenson DK (2004) Tau induces cooperative Taxol binding to microtubules. *Proceedings of the National Academy of Sciences* 101:12910–12915

Seabold S, Perktold J (2010) Statsmodels: Econometric and statistical modeling with python. *In: Proceedings of the 9th Python in Science Conference*. Austin, TX, pp 10–25080

Setru SU, Gouveia B, Alfaro-Aco R, Shaevitz JW, Stone HA, Petry S (2021) A hydrodynamic instability drives protein droplet formation on microtubules to nucleate branches. *Nature Physics* 17:493–498

Shima T, Morikawa M, Kaneshiro J, Kambara T, Kamimura S, Yagi T, Iwamoto H, Uemura S, Shigematsu H, Shirouzu M, *et al.* (2018) Kinesin-binding–triggered conformation switching of microtubules contributes to polarized transport. *Journal of Cell Biology* 217:4164–4183

Sofroniew N, Lambert T, Evans K, Nunez-Iglesias J, Bokota G, Winston P, Peña-Castellanos G, Yamauchi K, Bussonnier M, Pop DD, *et al.* (2022) napari: a multi-dimensional image viewer for Python. *Zenodo*

Schmidt JC, Arthanari H, Boeszoermenyi A, Dashkevich NM, Wilson-Kubalek EM, Monnier N, Markus M, Oberer M, Milligan RA, Bathe M, *et al.* (2012) The kinetochore-bound Ska1 complex tracks depolymerizing microtubules and binds to curved protofilaments. *Developmental Cell* 23:968–980

Tanaka N, Meng W, Nagae S, Takeichi M (2012) Nezha/CAMSAP3 and CAMSAP2 cooperate in epithelial-specific organization of noncentrosomal microtubules. *Proceedings of the National Academy of Sciences* 109:20029–20034

Terpilowski MA (2019) scikit-posthocs: Pairwise multiple comparison tests in Python. *Journal of Open Source Software* 4:1169

Toya M, Kobayashi S, Kawasaki M, Shioi G, Kaneko M, Ishiuchi T, Misaki K, Meng W, Takeichi M (2016)

CAMSAP3 orients the apical-to-basal polarity of microtubule arrays in epithelial cells. *Proceedings of the National Academy of Sciences* 113:332–337

Williamson T, Gordon-Weeks PR, Schachner M, Taylor J (1996) Microtubule reorganization is obligatory for growth cone turning. *Proceedings of the National Academy of Sciences* 93:15221–15226

Yajima H, Ogura T, Nitta R, Okada Y, Sato C, Hirokawa N (2012) Conformational changes in tubulin in GMPCPP and GDP-taxol microtubules observed by cryoelectron microscopy. *Journal of Cell Biology* 198:315–322

Zanic M, Widlund PO, Hyman AA, Howard J (2013) Synergy between XMAP215 and EB1 increases microtubule growth rates to physiological levels. *Nature Cell Biology* 15:688–693

Zhang R, LaFrance B, Nogales E (2018) Separating the effects of nucleotide and EB binding on microtubule structure. *Proceedings of the National Academy of Sciences* 115:E6191–E6200

Zhang R, Roostalu J, Surrey T, Nogales E (2017) Structural insight into TPX2-stimulated microtubule assembly. *Elife* 6:e30959

713 **Figure legends**

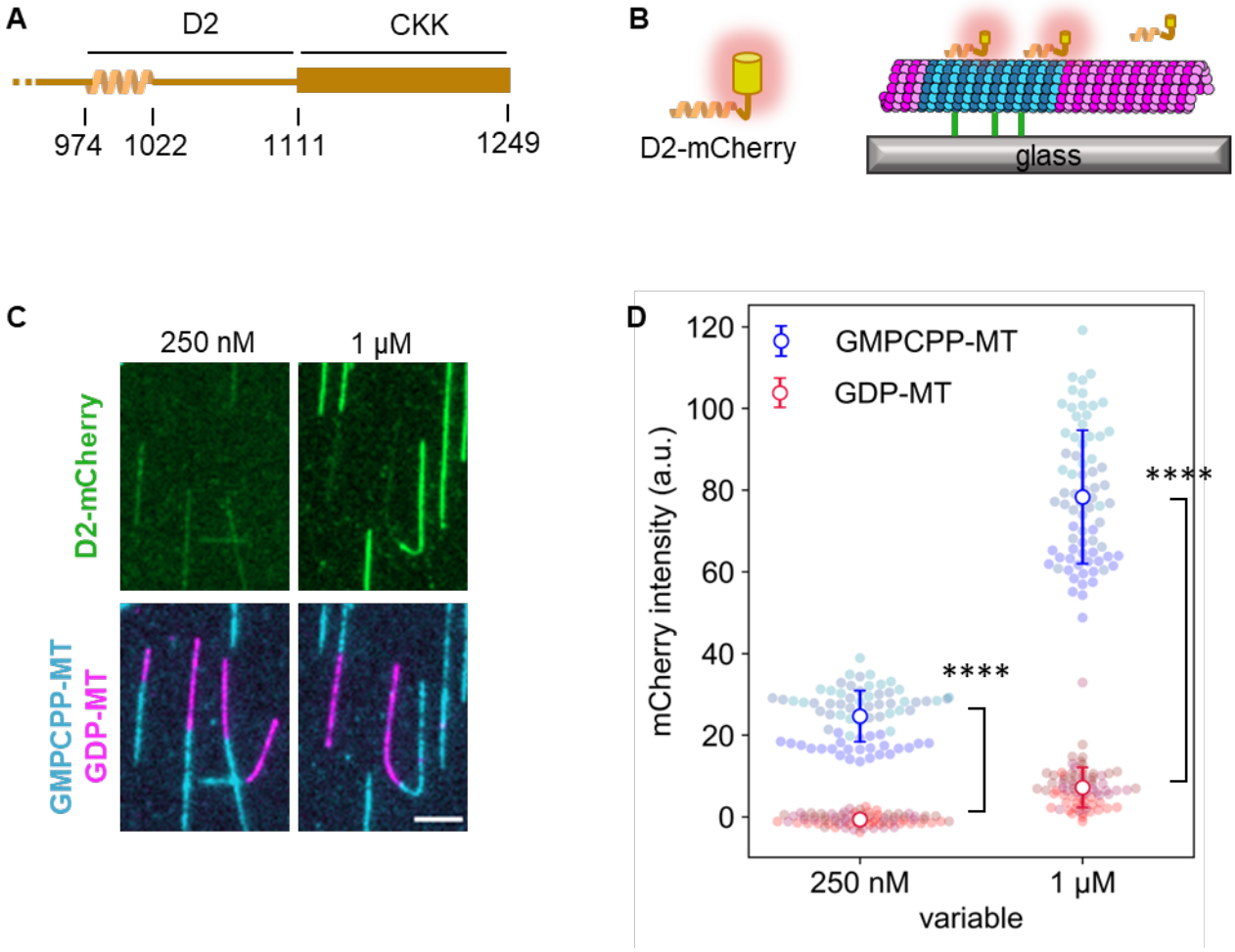

714

715 **Fig. 1**: The D2 region in CAMSAP3 prefers GMPCPP-stabilized microtubules. (**A**) A schematic of human
716 CAMSAP3 at its C-terminal. (**B**) A schematic of the TIRF microscopy used in the binding assay. The
717 depolymerization of GDP-MTs was inhibited by adding 25% glycerol in the imaging buffer. We avoided using
718 taxol in this assay because of its effects on the microtubule lattice. Blue indicates the GMPCPP-stabilized
719 microtubule seed. Magenta shows GDP-MT elongated from the seed. (**C**) Representative images showing D2
720 binding to microtubules. Contrasts are set to the same range for each channel. Images after unmixing the
721 fluorescence intensities are shown. Scale bar, 5 μm. 75 GMPCPP-MTs and 75 GDP-MTs from three replicates
722 were analyzed for each D2 concentration. (**D**) Quantification of the average fluorescence intensity of D2-
723 mCherry along microtubules. Colors represent three replicates. Error bars, S.D. ****: $p < 0.0001$ (Welch's t-
724 test).

725

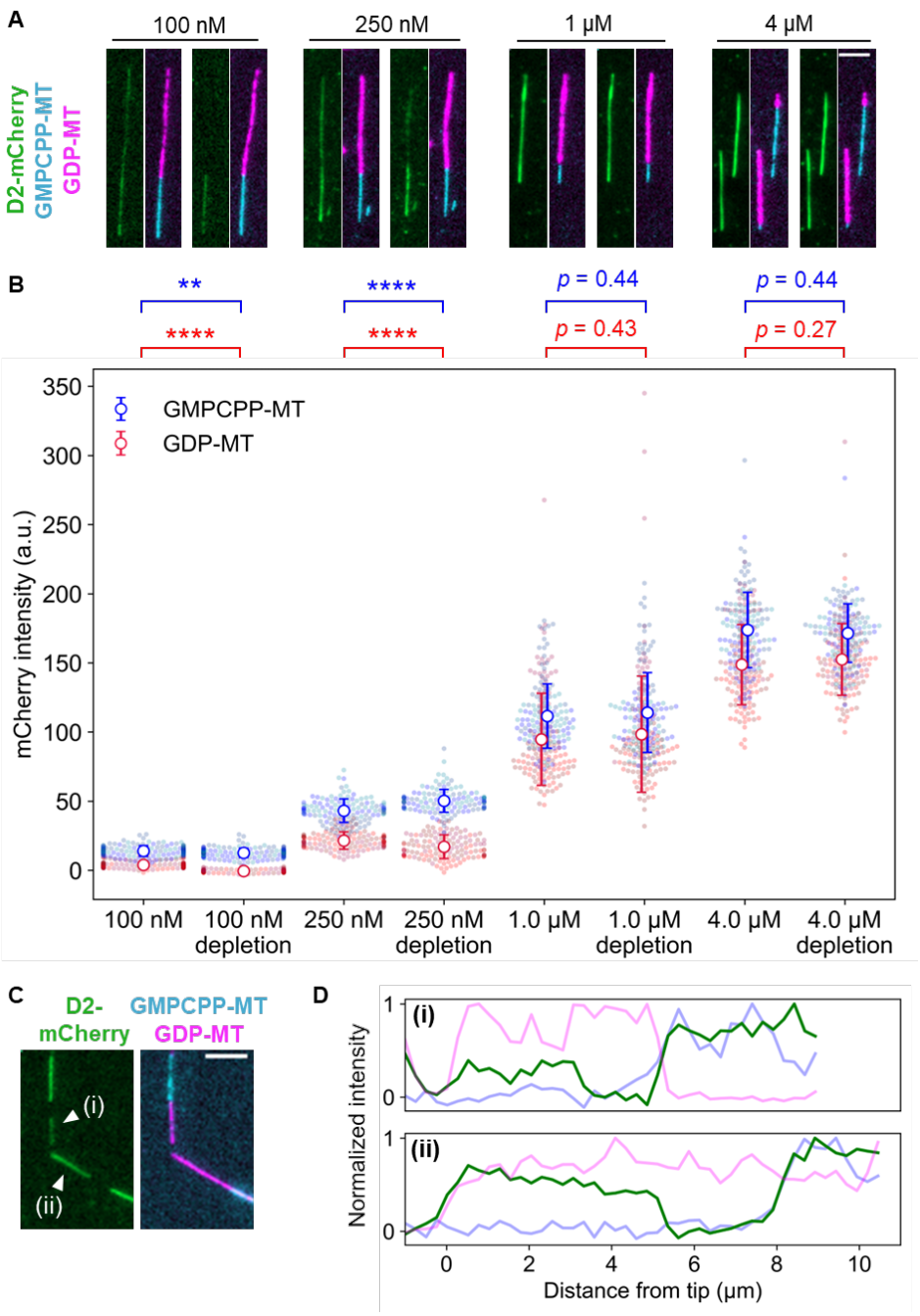

Fig. 2: The affinity of D2 to GDP-MT was enhanced by the addition of taxol. (**A**) Representative images of D2 binding to microtubules in the presence of taxol (left sides) or after 5-min taxol depletion (right sides). Contrasts were set to the same range for each concentration to highlight the difference before and after taxol-depletion. Scale bar, 5 μm. (**B**) Quantification of average fluorescence intensities of D2-mCherry. Error bars, S.D. **: $p < 0.01$, ****: $p < 0.0001$ (Welch's t-test). Cohen's d after taxol depletion was $d = 2.4$ for 100 nM D2 and 0.60 for 250 nM D2. The mean value and sample size of each data set is summarized in Table 1. (**C**) Representative images of D2-rich subregions [marked as (i) and (ii)] on GDP-MT at 250 nM D2 after taxol-depletion. Scale bar, 5 μm. (**D**) Line profiles of microtubules in (C) plotted against the distance from the tips.

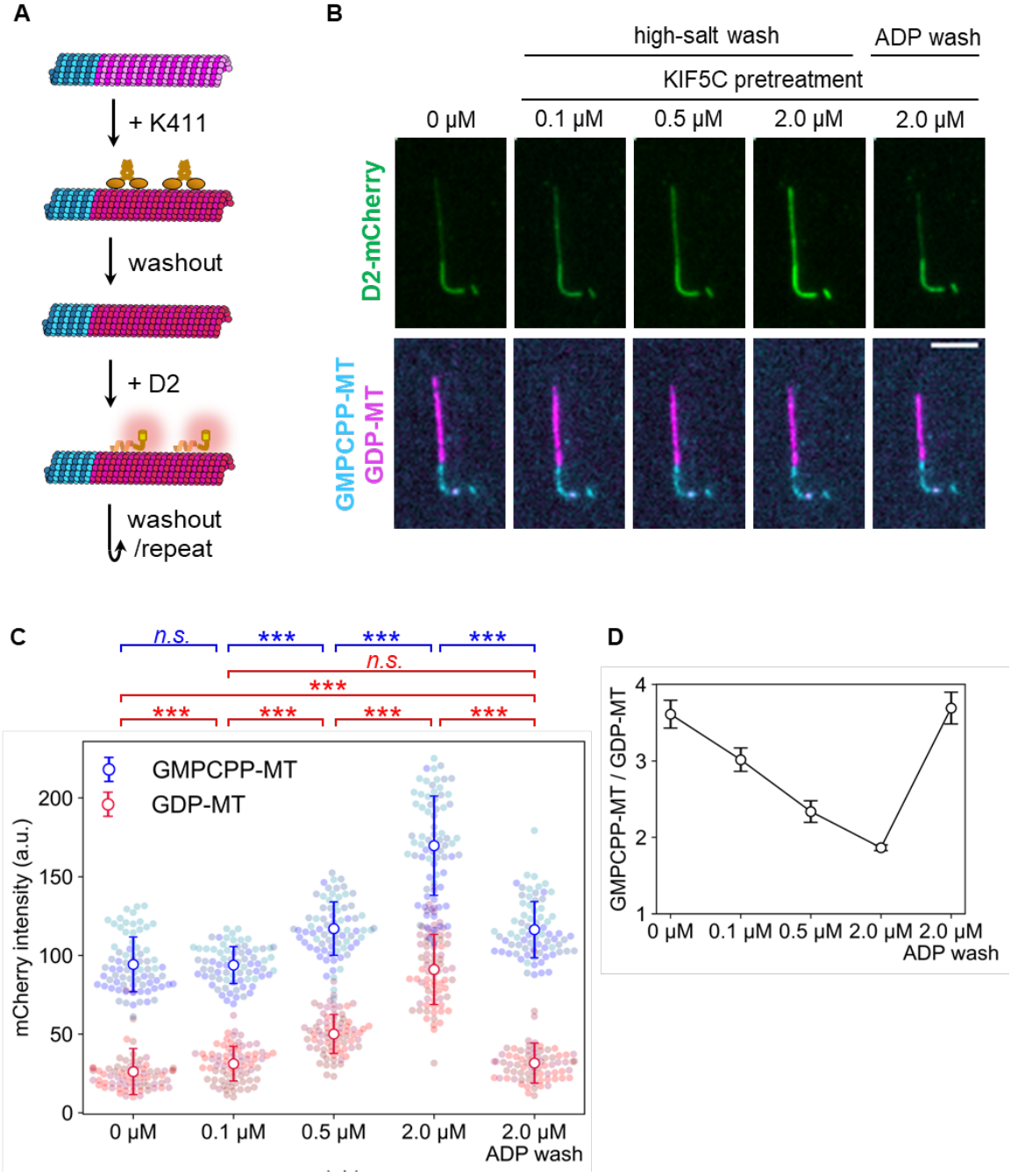

Fig. 3: Microtubule expansion by KIF5C pre-treatment promotes D2-binding. (**A**) Overview of the KIF5C pre-treatment assay. Coloring is the same as in Fig. 1B except for the expanded GDP-MT lattice shown in red. KIF5C was added to induce microtubule expansion and washed out before applying D2. (**B**) Representative images after adding D2. Contrasts are set to the same values for each channel. Scale bar, 5 μm. (**C**) Quantification of D2-mCherry fluorescence intensity on microtubules. Colors indicate different replicates. Error bars, S.D. ***: $p < 0.001$ (Steel-Dwass test); n.s., not significant. Sample size of each data set is summarized in Table 2. (**D**) Binding specificity of D2. Specificity was calculated as the mCherry intensity ratio on GMPCPP-MT to that on GDP-MT. Error bars are the standard error predicted by pairs of standard errors in (C) and the error propagation rule.

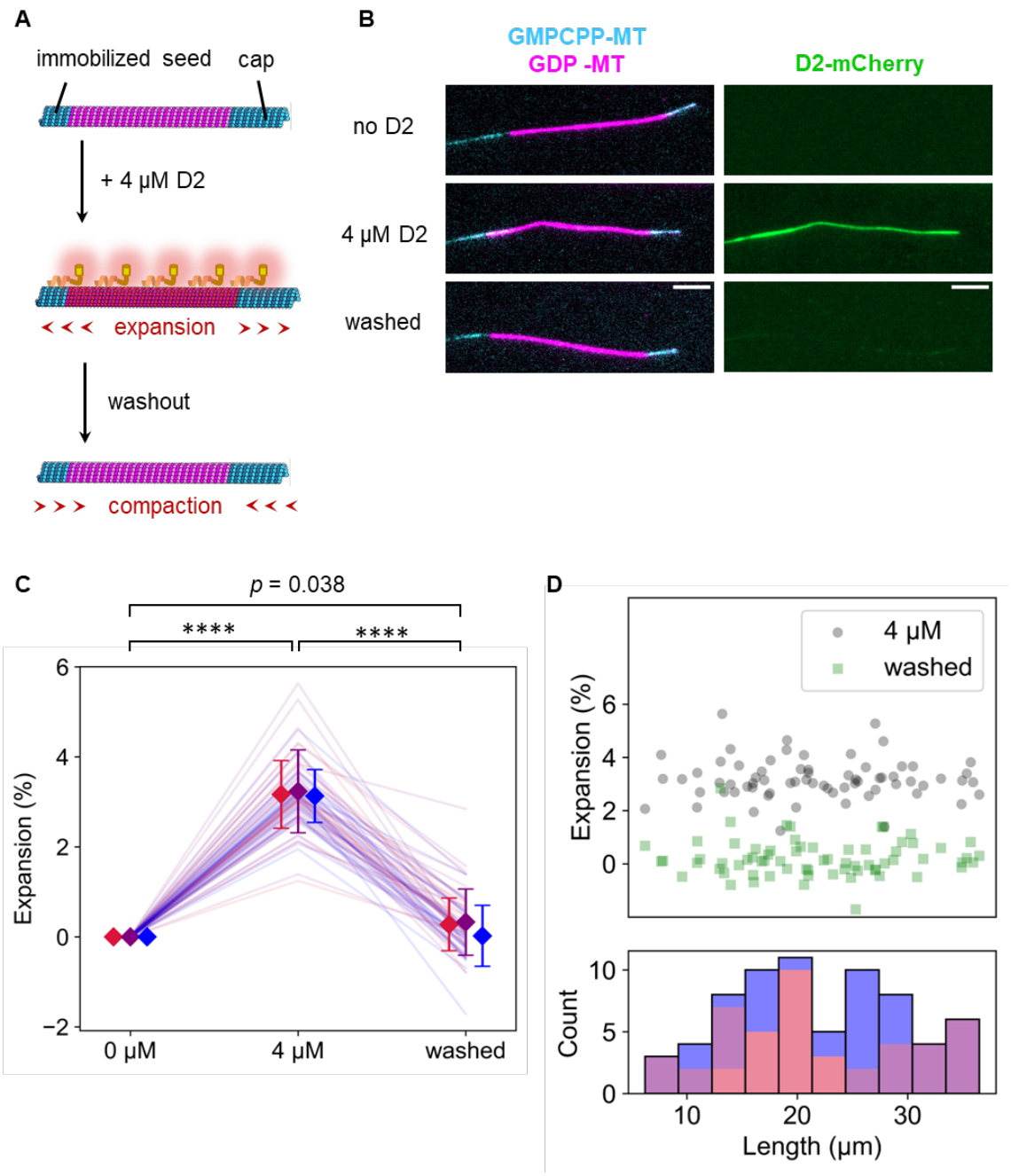

Fig. 4: Microtubule lattice expansion triggered by D2-binding. (**A**) Schematic illustration of the assay. Coloring is the same as in Fig. 3A. (**B**) Representative images during the expansion assay. Red-to-green and green-to-blue fluorescence leakage were unmixed. Scale bar, 5 μm. (**C**) Quantification of the normalized microtubule length between Alexa Fluor 488-labeled GMPCPP seed and Alexa Fluor 488-labeled GMPCPP-capped microtubules. Microtubule length was calculated by 2D Gaussian fitting of the total intensity and spline fitting in the Cy5 channel. Each color represents a different replicate. Error bars indicate mean and S.D. of each replicate. ****: $p < 0.0001$ (paired t-test with Bonferroni correction). 69 microtubules from three replicates were analyzed. (**D**) Scatter plot between the expansion rate and the microtubule lengths (upper) and a stacked histogram of the lengths in the 0 μM D2 condition (bottom). Each color corresponds to the same replicate in (C).

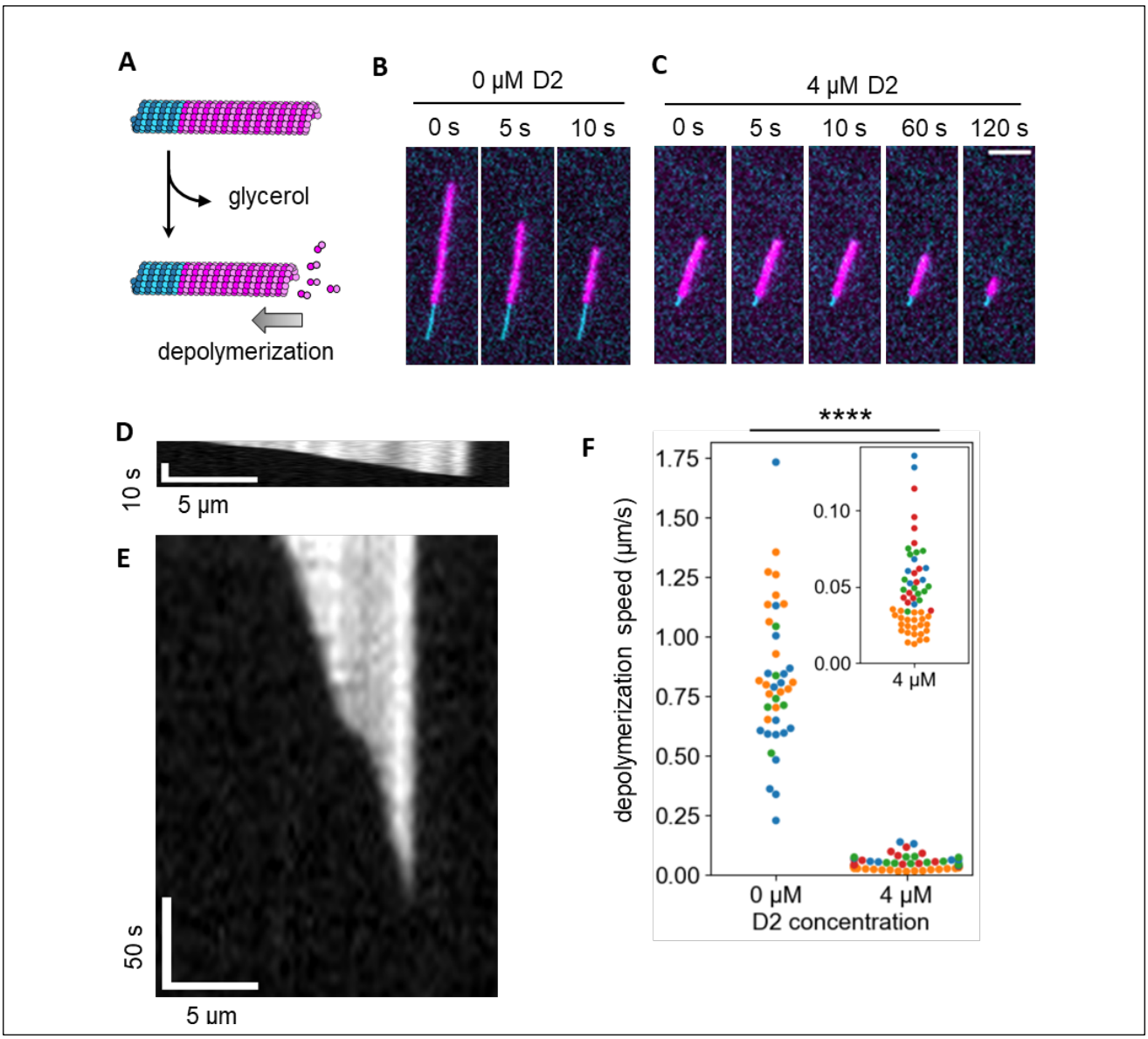

757

758 **Fig. 5**: Microtubule depolymerization was suppressed by D2-binding. (**A**) Schematic illustration of the assay.
759 Microtubule depolymerization was induced by replacing the buffer with glycerol-free buffer. (**B, C**)
760 Representative frames during depolymerization without D2 (B) or with 4 μM of D2 (C). The cyan channel
761 image (GMPCPP seed) was taken only at the first frame so that the same image was used for each frame. Scale
762 bar, 5 μm. (D, E) Kymographs of the microtubules in (B) and (C), respectively, depolymerizing without D2 (**D**)
763 or with 4 μM D2 (**E**). Since the images were taken at different time intervals, two kymographs were resized to
764 fit the same time scale. (**F**) Microtubule depolymerization speed. Different colors represent different replicates.
765 0 μM: 0.82 ± 0.30 μm/s (mean ± S.D., 40 microtubules, 3 replicates); 4 μM: 0.046 ± 0.028 μm/s (mean ± S.D.,
766 56 microtubules, 4 replicates). ****: $p < 0.0001$ (Welch's t-test).

767

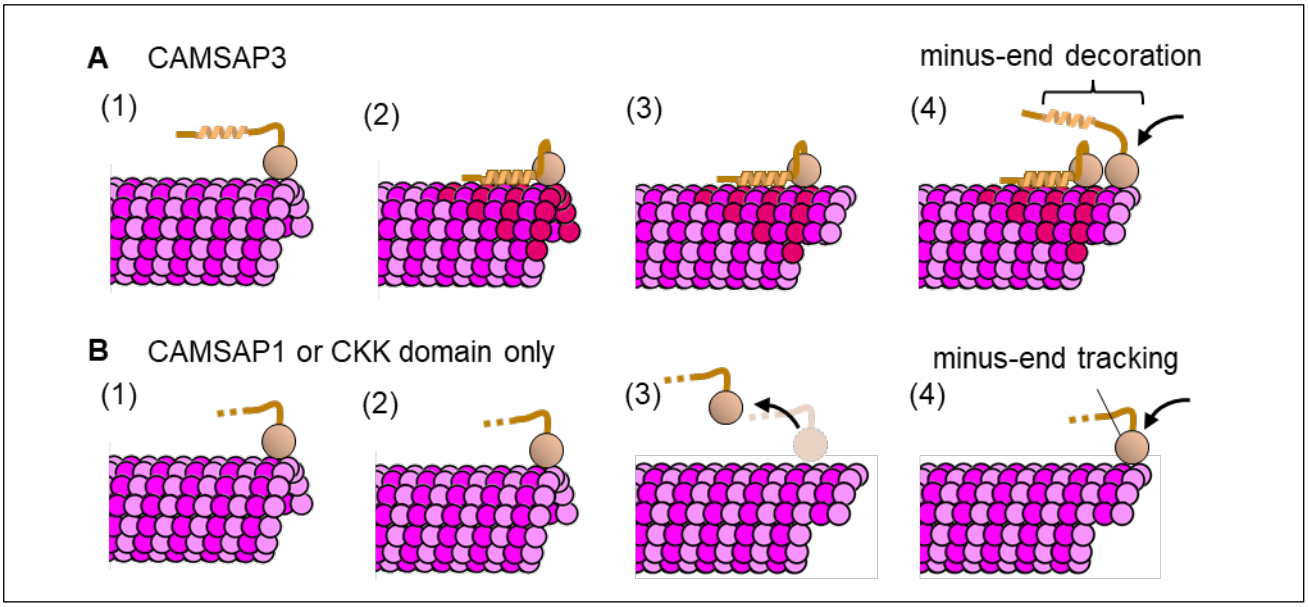

Fig. 6: Model of minus-end decoration and stabilization by CAMSAP3 and comparison with CAMSAP1. (A) CAMSAP3 can specifically bind to the microtubule minus end owing to its CKK domain (1), and the adjacent D2 region expands the microtubule lattice (2). The strong interaction between D2 and expanded microtubule (red tubulins) keeps CAMSAP3 molecules bound on the microtubule surface even after the microtubule is polymerized (3). The newly formed minus end provides additional binding sites for other CAMSAP3 proteins (4). This mechanism was observed as minus-end "decoration" under TIRF microscopy. (B) CAMSAP1 can specifically bind to the microtubule minus end (1) but has no effect on the microtubule lattice structure (2). Upon polymerization (3), CAMSAP1 dissociates from the microtubule because where it bound is no longer a minus end. The newly formed minus end is open to CAMSAP1 proteins so that CAMSAP1 appears to be "tracking" the minus end.

781 **Tables**

782

783 **Table 1**: mCherry intensity on microtubules in the taxol-depletion assay.

Condition		mCherry intensity (a. u., mean ± S.D.)			
Microtubule	Taxol	100 nM	250 nM	1 μM	4 μM
GMPCPP-MT	20 μM	14 ± 4 (n = 150)	43 ± 9 (n = 130)	112 ± 23 (n = 130)	173 ± 27 (n = 130)
	Depleted	13 ± 3 (n = 150)	50 ± 8 (n = 130)	114 ± 29 (n = 130)	171 ± 21 (n = 130)
GDP-MT	20 μM	4.0 ± 2.4 (n = 150)	22 ± 6 (n = 130)	95 ± 33 (n = 130)	148 ± 29 (n = 130)
	Depleted	-0.5 ± 1.1 (n = 150)	17 ± 8 (n = 130)	98 ± 41 (n = 130)	152 ± 25 (n = 130)

784

785 **Table 2**: mCherry intensity on microtubules in the kinesin pre-treatment assay.

KIF5C concentration	mCherry intensity (a. u., mean ± S.D.)		GMPCPP/GDP (mean ± S.E.)
	GDP-MT	GMPCPP-MT	
0 μM	26 ± 15 (n = 75)	94 ± 17 (n = 75)	3.61 ± 0.18
0.1 μM	31 ± 11 (n = 75)	93 ± 12 (n = 75)	3.02 ± 0.15
0.5 μM	50 ± 12 (n = 75)	117 ± 17 (n = 75)	2.34 ± 0.14
2 μM	91 ± 22 (n = 75)	170 ± 32 (n = 75)	1.86 ± 0.04
2 μM (ADP wash)	32 ± 13 (n = 75)	116 ± 18 (n = 75)	3.69 ± 0.21

786

Supplementary Information

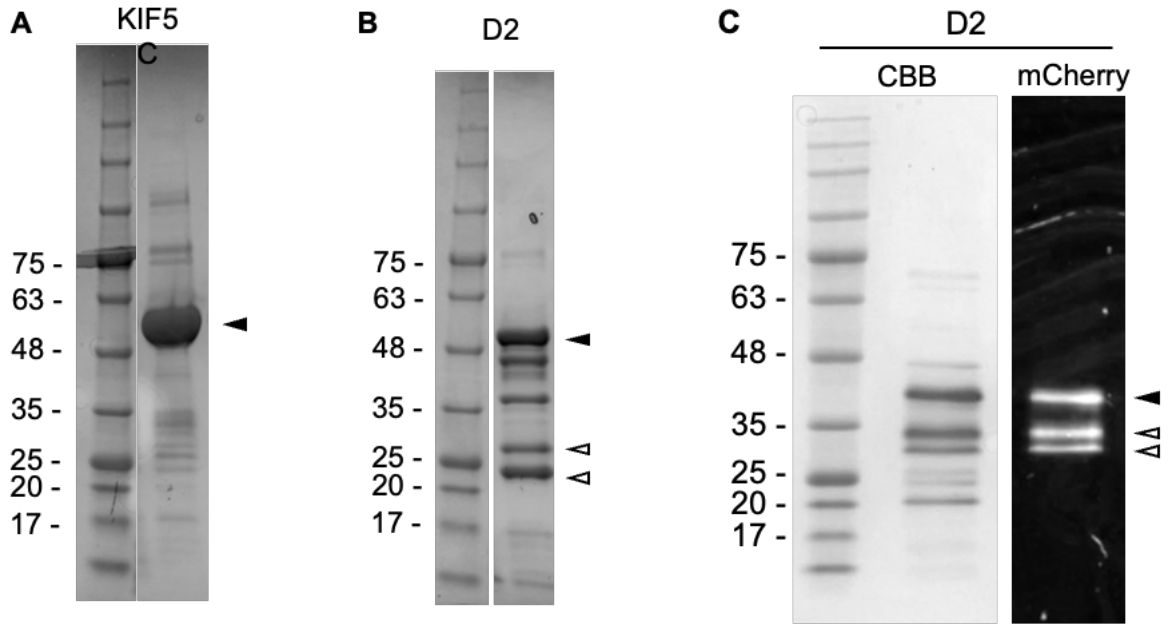

Fig. S1: SDS-PAGE gel images of purified KIF5C (**A**), boiled D2-mCherry (**B**) and non-boiled D2-mCherry (**C**). The black arrowheads indicate the bands corresponding to the proteins of interest. The bands indicated by the white arrowheads in the boiled sample (B) are considered fragments of D2-mCherry, because heating by the SDS-PAGE loading buffer splits mCherry. A non-boiled D2 sample (C) was analyzed on SDS-PAGE with CBB staining (left) and mCherry fluorescence (right). The lower mCherry bands (white arrowheads) were attributed to the fragmentation of D2 during the expression and purification processes so that they were not calculated as active fractions. Since purification of the C3 region (D2 + C-terminal CKK domain) of mouse CAMSAP3 also resulted in multiple SDS-PAGE bands in previous work (Fig. S4 of Jiang *et al.*, 2014), we considered this low purity (~0.6) to be inevitable for this protein construct.

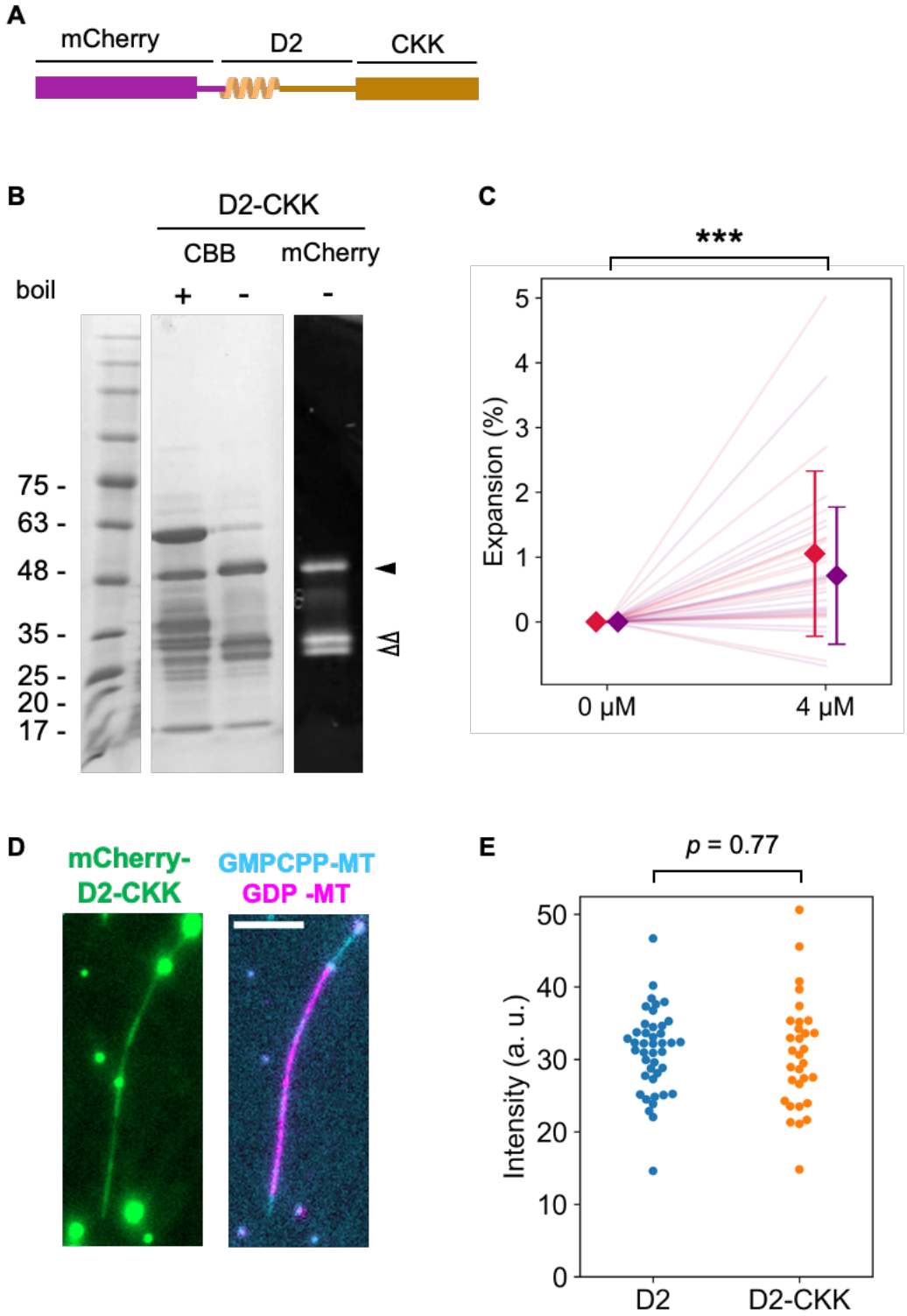

Fig. S2: Quantification of GDP-MT expansion by D2-CKK. (**A**) The D2-CKK gene was inserted into the pCold I (3361; TAKARA Bio) vector with the N-terminal 6xHis-tag and mCherry sequence and transformed into BL21 (DE3) competent cells. The construct was expressed and purified using the same procedure as the D2 construct, with two modifications. First, protein expression was induced by overnight incubation at 12°C since pCold vector requires lower temperature for the induction. Second, after mixing the crude extract with Ni-NTA agarose resin, the resin was washed with wash buffer (50 mM Tris-Cl, 500 mM NaCl) containing gradually increasing

807 concentration of imidazole (2 column volumes (CVs) of 10 mM, 2 CVs of 50 mM, 4 CVs of 100 mM and 4
808 CVs of 150 mM imidazole) and the last fraction was collected and used for experiments. (**B**) SDS-PAGE gel
809 images of the purified D2-CKK. Same as in the case of Fig. S1, a non-boiled sample was analyzed to determine
810 protein purity (~0.6). The bands corresponding to the full length and fragments of the construct are indicated
811 with the black and white arrowheads, respectively. (**C**) Microtubule expansion assay using D2-CKK. The assay
812 was carried out using the same protocol as for D2 (Fig. 4C). The different colors indicate the two replicates of
813 the assay. Diamonds and bars indicate the mean and S.D. of each replicate, respectively. ***: $p < 0.001$ (paired
814 t-test). 33 microtubules from two replicates were analyzed. (**D**) Representative images of a microtubule
815 expanded by 4 μM D2-CKK. At this concentration, D2-CKK bound along the entire length of the microtubule,
816 similar to D2 (Figure 4). Bright aggregates were observed even in the supernatant of a centrifugation at 20,000
817 x g, 3 min, 4°C. Scale bar, 5 μm. (**E**) Distribution of the mCherry fluorescence intensity on each microtubule in
818 the expansion assays with 4 μM D2 or D2-CKK. The median value of the intensity along each microtubule was
819 plotted to exclude the effect of the bright aggregates. Judging from the intensity, there was no significant
820 difference between D2 and D2-CKK in the amount of binding to microtubules ($p = 0.77$, Welch's t-test). From
821 the assays with D2 and D2-CKK, 42 and 31microtubules were analyzed, respectively.
822
823

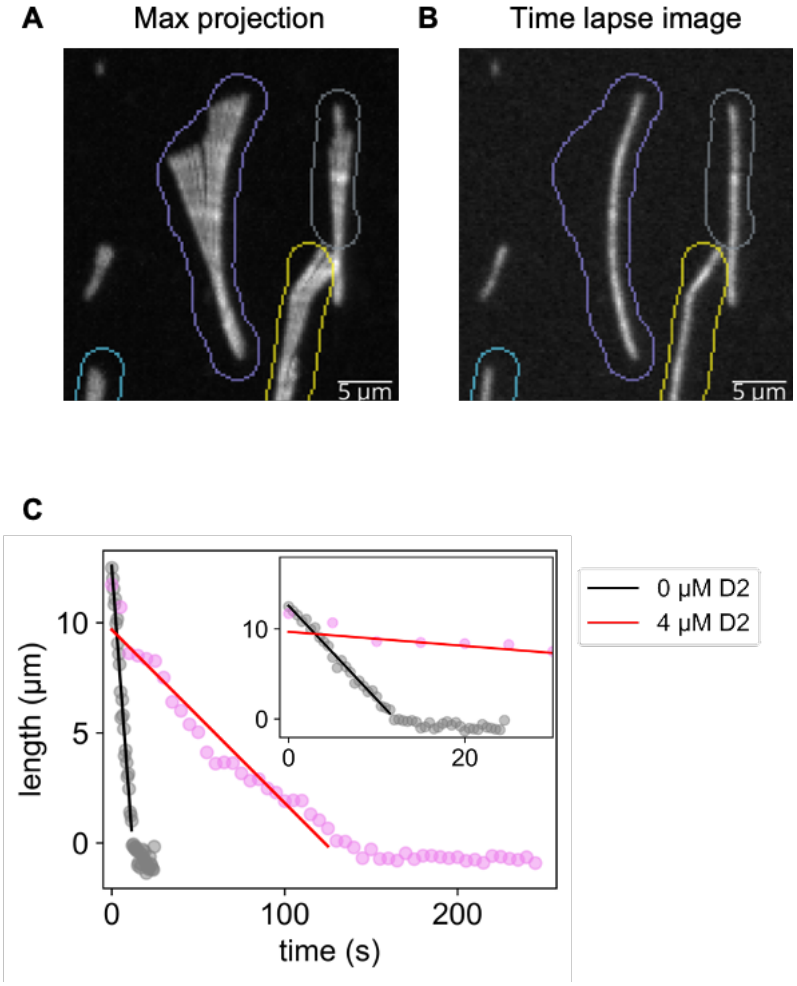

Fig. S3: Quantification of the depolymerization rate of microtubules that were shaking during the image acquisition. (**A**) Image labels that enclose a microtubule were manually drawn. Colored pixels are the contours of labels. Different colors indicate different labels. (**B**) Overlay of the label contour and time lapse image at t = 0. (**C**) Representative plots of the microtubule length against the imaging time and corresponding results of the linear regression. Length was calculated by associating the fluorescence intensity and microtubule length at t = 0.

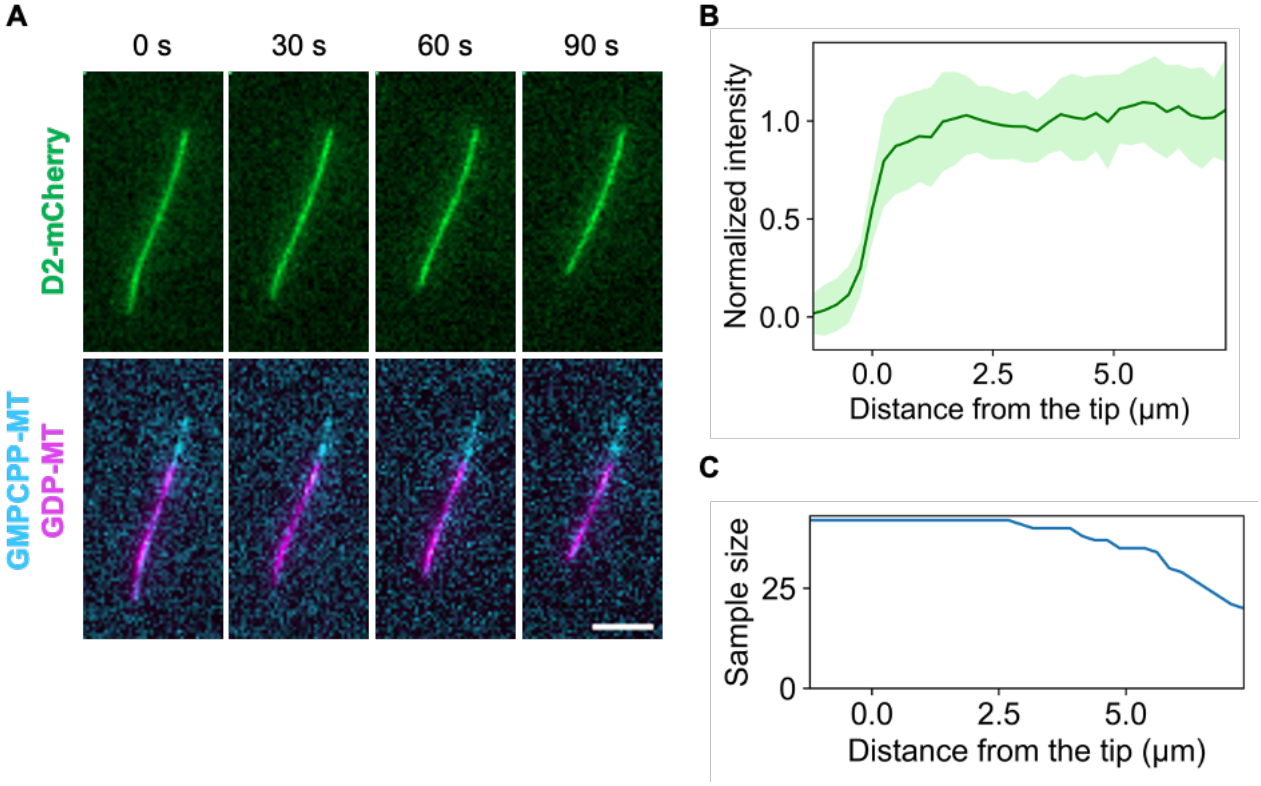

Fig. S4: Inspection of depolymerizing microtubules reveals that D2 does not accumulate on the tips. (**A**) Representative frames during depolymerization, where D2-mCherry was also visualized. Scale bar, 5 μm. (**B**) Averaged line profiles from the microtubule tips (mean ± S. D.). 11 microtubules from three replicates were selected, and three or four frames were used for each microtubule. (**C**) Sample size profile (n = 42 at the maximum). Due to the presence of short microtubules, the sample size decreased over 2.5 μm.

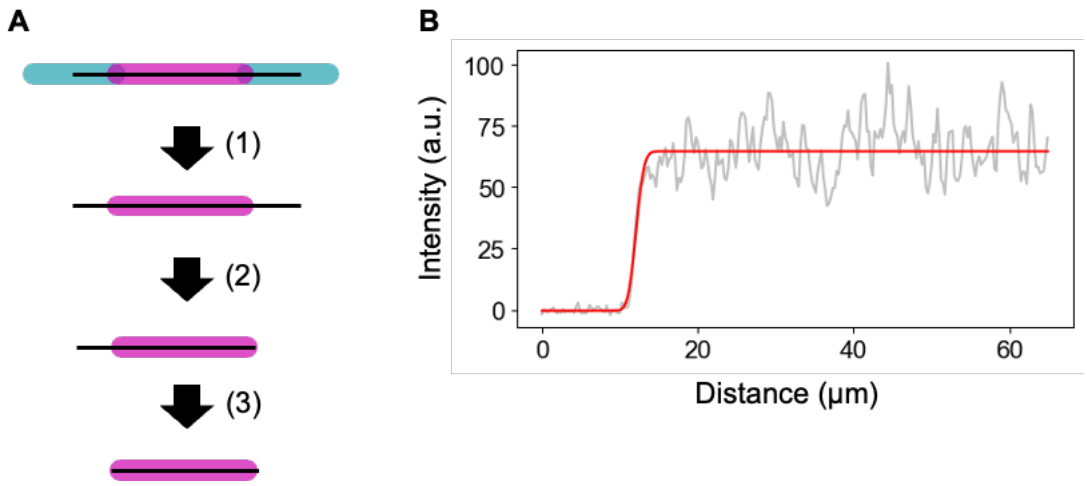

Fig. S5: Illustration of the measurement of microtubule length. (**A**) The microtubule center line was determined from the total intensity, and the length of the Cy5-labeled microtubule was calculated by fitting the line profile to the error function on each tip. (**B**) An example of fitting the error function to data for one tip.